Design and improvement of plasmonic nanostructure enhanced photovoltaic solar cell with alternative materials

by

Fariha Alam Urbana(200021315)

Jarin Tasnim Rahman(200021316)

M. Sadman Aster(200021344)

A Thesis Submitted to the Academic Faculty in Partial Fulfillment of the Requirements for the Degree of

BACHELOR OF SCIENCE IN ELECTRICAL AND

ELECTRONIC ENGINEERING

Department of Electrical and Electronic Engineering

Islamic University of Technology (IUT)

Gazipur, Bangladesh

October 2025

Declaration of Authorship

We hereby certify that the thesis titled “Design and improvement of plasmonic nanostructure enhanced photovoltaic solar cell with alternative materials ”represents the outcome of research conducted under the supervision of Dr. Rakibul Hasan Sagor, Professor at the Islamic University of Technology. This work fulfills partial requirements for the degree of Bachelor of Science in Electrical and Electronic Engineering at IUT.

We affirm that this thesis or any part of it, has not been previously submitted for any other degree or diploma. Proper attribution has been given to all consulted sources and published works of others.

Signatures of the Candidates

—---

Fariha Alam Urbana

Student ID: 200021315

—---

Jarin Tasnim Rahman

Student ID: 200021316

—--

M. Sadman Aster

Student ID: 200021344

Certificate of Approval

Design and improvement of plasmonic nanostructure enhanced photovoltaic solar cell with alternative materials

Submitted by

Fariha Alam Urbana(200021315)

Jarin Tasnim Rahman(200021316)

M. Sadman Aster(200021344)

has been approved by:

Dr. Rakibul Hasan Sagor

Supervisor and Professor,
Department of Electrical and Electronic Engineering,
Islamic University of Technology (IUT),
Boardbazar, Gazipur-1704.

Date: ………………….

Acknowledgement

Firstly, we extend our sincere gratitude to the Almighty Allah for granting us the strength and perseverance to complete this thesis. We deeply appreciate the invaluable guidance and unwavering support of Prof. Dr. Rakibul Hasan Sagor, whose insights and encouragement were instrumental in shaping our research.

We also thank Mr. A. K. M. Rakib for his early guidance and teachings which laid a strong foundation for our work. Our heartfelt thanks go to all faculty members of the Electrical and Electronic Engineering Department at IUT for their support and inspiration throughout our academic journey.

Lastly, we are grateful to our families for their unwavering support, understanding and belief in our abilities.

Fariha Alam Urbana
Jarin Tasnim Rahman
M. Sadman Aster

October, 2025

Table of Contents

Declaration of Authorship **2**
Acknowledgement **4**
List of Tables **7**
List of Figures **8**
Abstract **9**
Introduction **10**
1.1 Thin-film interference and Bragg (quarter-wave) design 11
1.2 Guided-mode resonance & photonic coupling 11
1.3 Scattering theory for nanostructures (Mie & dipole approximations) 12
1.4 Localized surface plasmon resonance (LSPR) and material permittivity 12
1.5 Near-field coupling, hybridization, and cluster/lattice effects 12
1.6 Lattice resonances, Rayleigh anomalies, and diffractive coupling 13
1.7 Parasitic loss, energy partitioning, and device-level considerations 13
1.8 Local density of optical states (LDOS) and absorption enhancement 13
Literature Review **15**
Proposed Designs of Bragg Stacks and 2×3 Spherical-Array Structures for Thin-Film Photovoltaic Light-Trapping **27**
3.1 Bragg (Quarter-Wave) Single-Material Stacks 27
Material dispersion and loss 27
3.2 Finite 2×3 Spherical Nanoparticle Array 29
Substrate influence and image effects 30
3.3 Material and Performance Considerations 30
Methodology **31**
4.1 Method of Simulation 31
4.1.1 Bragg (alternating-layer) — single-material cases 31
4.1.2 Spherical-array — finite 2×3 cluster (generic procedure) 33
4.2 Lumerical FDTD implementation — detailed procedure and best practices 39
4.3 Lumerical FDTD implementation Computational Strategies and Equations 41
Result Discussion and Analysis **43**
5.1 . Bragg Stack Design (Alternating Layered Structure) 43
5.1.1 Overview of the Bragg Structure 45
5.1.2 Material-Specific Performance (From Figure 5.1) 45
5.1.3 Material Pair Performance (From Figure 2 —Figure5.2) 46
5.1.4 Comparative Design Behavior (Design 1 vs. Design 2) 47
5.1.5 Overall Alternating Stack Analysis (From Figure 3) 47
5.2 Spherical Array Design 48
5.2.1:Optical Performance of Spherical Arrays 49

5.2.2 Comparative Discussion 50
5.3:Optical Performance of 2x2 Pyramid Arrays 50
5.4 Summary 51
Fabrication process and experimental setup **53**
6.1 Introduction 53
6.2 Numerical Simulation Framework 53
6.3 Experimental Setup for Bragg and Spherical Systems 54
6.3.1 Bragg Stack Resonator Setup 54
6.3.2 Spherical Array Resonator Setup 55
6.4 Fabrication Methodology 55
6.4.1 Substrate Preparation 55
6.4.2 Material Deposition 55
6.5 Fabrication Process for Bragg Resonator Arrays 56
6.6 Fabrication Process for Spherical Array Structures 57
Fabrication Process 58
6.7 Characterization Techniques 58
6.8 Summary 59
Conclusion **60**
1 Demonstration of Outcome Based Education (OBE) **62**
8.1 Introduction 62
8.1.1 Course Outcomes (COs) Addressed 62
8.1.2 Aspects of Program Outcomes (POs) Addressed 63
8.1.3 Knowledge Profiles (K3 – K8) Addressed 65
8.1.4 Use of Complex Engineering Problems 66
8.2 Socio-Cultural, Environmental, And Ethical Impact 67
8.3 Attributes of Ranges of Complex Engineering Problem Solving (P1 – P7) Addressed 67
8.4 Attributes of Ranges of Complex Engineering Activities (A1 – A5) Addressed 69
References **71**

List of Tables

Table 2.1 Detailed summary of the reviewed literature 15

List of Figures

Figure 1.1 Propagation of SPP along metal-dielectric interface 2

Figure 3.1: Alternating stack design(6 blocks) 28

Figure 3.2 : 2x3 Spherical Array 30

Figure 4.1: Alternating stack design(monitor view) 33

Figure 4.2: 2x3 Spherical Array (monitor -side view) 34

Figure 4.3: 2×2 Spherical Array (monitor-side view) 36

Figure 4.3: 4×3 Spherical Array (monitor -side view) 38

Figure 4.4: 2×2 Pyramidal Array (monitor -side view) 39

Figure 5.1: Alternating Bragg resonator output 45

Figure 5.2: Alternating Bragg resonator output with a single material 45

Figure 5.3: Alternating Bragg resonator output with a single material and material pair 46

Figure 5.4: 2x2 Spherical array output 51

Figure 5.5:2x3 Spherical array output 51

Figure 5.6: 2x2 Pyramidal array output 53

Abstract

Improving the efficiency of solar cells have been intensified by the growing global energy demand and the increasing need for sustainable power generation . Among various approaches, Nanostructured light-trapping techniques, among various approaches have emerged as an effective way to boost the performance of thin-film and silicon-based photovoltaics. Enhancement of optical absorption and overall energy conversion have made plasmonic and photonic nanostructures particularly more promising. They can confine, scatter, and redirect light within the active region of a solar device.

Gold (Au) and silver (Ag) have demonstrated remarkable optical properties as being the traditional plasmonic materials , yet their high cost, intrinsic losses, and incompatibility with standard semiconductor fabrication processes limit their practical application. Recent studies have turned toward alternative plasmonic materials that are both low-loss and CMOS-compatible; to address these issues .

In this work, the optical response of alternative plasmonic materials have been focused, including titanium nitride (TiN), zirconium nitride (ZrN), tin (Sn), and titanium dioxide (TiO_2), while exploring their potential for efficient light trapping in the near-infrared region. To analyze two design configurations: a multilayer dielectric Bragg reflector that relies on wave interference, and finite spherical nanoparticle arrays (2×3 and 2×2) that utilize near-field coupling effects; Finite-difference time-domain (FDTD) simulations are used. The comparative analysis have provided us with the insights into how these material–structure combinations can enhance light absorption in silicon-based systems and contribute to the development of low-cost, sustainable, and high-efficiency photovoltaic technologies.

Chapter 1

Introduction

Photovoltaic (PV) technology has emerged as a cornerstone of the global transition to low-carbon energy, driven by rapid deployment, steady improvements in cell efficiency, and maturation of manufacturing routes. Despite these gains, the levelized cost of solar electricity remains a key barrier to even broader adoption in many markets; consequently, reducing the cost per watt produced is a central objective of contemporary PV research[1]. While balance-of-system and installation costs are important, materials and processing frequently comprise a substantial portion of module expense—motivating strategies that maintain or improve optical absorption while dramatically reducing the volume of active semiconductor.[2]

Thin-film photovoltaics address this challenge by replacing thick crystalline wafers with micron-scale absorbers deposited on inexpensive substrates. This reduction in material use has enabled economically attractive alternative absorbers (for example, CdTe and chalcopyrite-based compounds) and simpler fabrication pathways, which together can lower manufacturing cost per watt. However, the thinner optical path also reduces single-pass absorption, making efficient light-trapping and careful optical design indispensable to preserve—or exceed—the performance of bulk devices.[3]

Nanophotonic approaches, including surface texturing, dielectric photonic stacks, and nanoscale scatterers, offer routes to substantially increase the effective optical path and to funnel light into guided or localized modes within ultrathin absorbers. In particular, engineered scattering elements and low-loss photonic layers can redirect incident sunlight into high-angle or in-plane wavevectors, enhance near-field intensity inside the absorber, and broaden angular acceptance—thereby recovering absorption without incurring significant parasitic losses. [4]Integrating these optical strategies with low-material-volume architectures therefore provides a pragmatic pathway to reduce cost per watt while maintaining high device efficiency.[5]

1.1 Thin-film interference and Bragg (quarter-wave) design

- **Quarter-wave principle:** Alternating high- and low-index layers each of optical thickness $\lambda_0/4$ produce constructive interference of reflections at the design wavelength λ_0, forming a photonic stop-band that strongly reflects and localizes light within the stack.

- **Reflectivity & stack engineering:** Reflectance of an N-period stack scales with index contrast and number of periods; high index contrast widens the stop-band and increases field enhancement in the dielectric spacer.

- **Impedance matching & coupling to substrate:** Tuning layer thicknesses and termination layers controls impedance seen by the incident wave, enabling selective coupling into substrate guided modes or maximizing reflection to boost scattering into the active layer.

1.2 Guided-mode resonance & photonic coupling

- **Guided-mode coupling:** A dielectric spacer (Si_3N_4 on Si) beneath a Bragg stack can support leaky guided modes. Evanescent overlap between the stack's localized fields and the waveguide mode enables energy transfer into in-plane propagation, increasing dwell time in the absorber.

- **Resonant lifetime & Q factor:** The quality factor of guided resonances determines how long light is stored; higher Q gives stronger field enhancement but narrower spectral bandwidth—important for broadband solar harvesting tradeoffs.

1.3 Scattering theory for nanostructures (Mie & dipole approximations)

- **Mie theory (spheres):** Exact solutions for scattering and absorption by spheres predict size- and index-dependent multipolar resonances (dipole, quadrupole), which set the single-particle extinction cross section σ_{ext}. For small particles (radius $\ll \lambda$) the dipole approximation suffices.

1.4 Localized surface plasmon resonance (LSPR) and material permittivity

- **Permittivity role (Re ε, Im ε):** Plasmon resonances require negative Re ε (metallic response) and are broadened by Im ε (ohmic losses). Materials with large |Re ε| and low Im ε (Ag in visible) produce sharp, high-field LSPRs but may be chemically/thermally less robust.

- **Figure of merit:** A useful figure of merit for plasmonic scatterers is |Re ε|/Im ε (or related quality factors), which quantifies the trade-off between field enhancement (from large negative Re ε) and parasitic absorption (from Im ε).

1.5 Near-field coupling, hybridization, and cluster/lattice effects

- **Dimer/cluster hybridization:** When two or more plasmonic particles approach within sub-wavelength gaps, their dipolar modes hybridize into bonding and antibonding combinations. Bonding modes concentrate charge in the gap and produce strong red- or blue-shifts depending on geometry.

- **Dual-peak behavior:** Hybridized clusters often display multiple peaks (shorter-wavelength bonding peaks and longer-wavelength collective or substrate-coupled peaks) because of competing local and radiative coupling channels.

1.6 Lattice resonances, Rayleigh anomalies, and diffractive coupling

- **Rayleigh anomalies:** Periodic arrays can produce diffractive coupling when a grating order becomes grazing (Rayleigh condition), enabling phase-matched excitation of in-plane modes and narrow lattice resonances that greatly enhance scattering at specific wavelengths.

- **Design knobs:** Pitch, fill factor, and refractive-index environment set the wavelength and strength of these resonances; coupling to guided modes in an underlying film can further increase absorption.

1.7 Parasitic loss, energy partitioning, and device-level considerations

- **Partition of extinction:** Extinction by a nanostructure splits into useful channels like scattering into absorber, coupling to guided modes and parasitic channels like absorption in the scatterer or non-absorbing layers. Minimizing Im ε and avoiding lossy metals where possible reduces parasitic heating.

- **Tradeoffs:** High scattering strength often coexists with increased parasitic absorption—optimal design balances scattering cross section, angular distribution, and material losses to maximize net absorption in the active layer.

1.8 Local density of optical states (LDOS) and absorption enhancement

- **LDOS impact:** Nanostructures and photonic stacks modify the local density of optical states near the absorber; increased LDOS at relevant wavelengths enhances spontaneous emission and absorption rates (Purcell-type effects) and therefore can improve light-matter interaction in ultrathin films.

- **Spectral/angle engineering:** Engineering LDOS and directional emission/scattering profiles broadens angular acceptance and improves integrated daily/seasonal energy collection.

Chapter 2

Literature Review

A comprehensive understanding of recent developments in nanostructured light-trapping and metasurface absorber technologies to be established, an in-depth review of several key studies has been conducted. Primarily focused studies on titanium nitride (TiN) and other refractory plasmonic materials exhibiting remarkable optical and thermal stability under high-temperature conditions; these studies have been concluded. Highlighting the ongoing transition from conventional noble-metal-based designs toward CMOS-compatible and cost-effective alternatives such as TiN, tungsten, and nickel; emphasis has been placed on the exploration of broadband absorption mechanisms, impedance matching strategies, and innovative nanostructural geometries that significantly enhance light-trapping efficiency and photothermal conversion performance. Moreover finite-difference time-domain (FDTD) modeling along with diverse simulation techniques, have been utilized to optimize design parameters and validate the optical behavior of proposed absorbers.Table **2.1** here represents a detailed summary of the reviewed literature, outlining the major design approaches, performance outcomes, and unique contributions of each study relevant to the present research work.

Table 2.1: Detailed summary of the reviewed literature

Name of the Paper	**Year**	**Main Findings**	**Novelty**	**Figure**	**Ref.**
Analysis of an ultra-broadband TiN-based metasurface absorber for solar thermophoto	2024	• Proposed Tin based metasurface absorber, high temp efficient working. • FDTD	The potential of Titanium Nitride as an absorbing material and developed a high-performance Metasurface Absorber(MA).which also works fine as a		[6]

voltaic cell in the visible to near infrared region		method ● Our analysis suggests that the MA can absorb more than 90% radiation in the 200–1733.5 nm range and achieves near-perfect absorbance (more than 99.5%) in the 719.7 - 1371 nm range which is suitable for solar cell applications. ● Maximum photothermal efficiency of 80% at	ME.removing the traditional noble metals drawback in high temperature.		

		1900 K			
Near-perfect spectrally-selective metasurface solar absorber based on tungsten octagonal prism array	2024	• The coupling effects of multi-plasmon resonance modes and the impedance matching lead to the high solar absorptivity. • The impedance mismatching is the mechanism to minimize the emissivity in the mid-IR region. • The excircle diameter of the first tungsten	A metasurface absorber consisting of an octagonal prism array is proposed, simple design and high photothermal efficincey	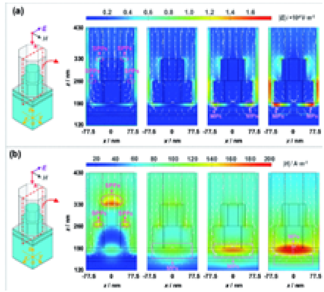 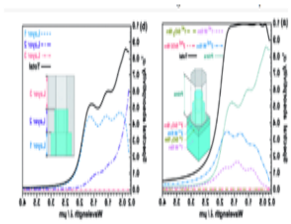	[7]

		octagonal prism and the height of SiO2 under the octagonal prism can influence the spectral absorptivity obviously. ● The metasurface absorber is demonstrated to be highly insensitive to both polarization and incident angles.			
Nano-resonator based broadband metamaterial absorber with angular stability		● The compact unit cell of the proposed absorber is formed by	The simple unique shape of the unit cell with rotational symmetry makes the suggested MMSA insensitive to the polarization angle on		[8]

operating in visible light spectrum for solar energy harvesting applications		three thin layers Nickel (Ni)-Silicon dioxide (SiO_2)-Nickel (Ni), its period is optimized as 400 nm ● the absorption over a bandwidth and the use of a less expensive metal are the main highlights and contributions	the one hand and the angular stability at oblique incidence up to 60° for both transverse electric (TE) and transverse magnetic (TM) modes on the other hand.		
Titanium nitride based plasmonic nanoparticles for photovoltaic application	2023	● Titanium nitride (TiN) nanoparticles demonstrated comparable	Demonstrating titanium nitride (TiN) as a high-performance, cost-effective alternative to noble metals like gold and silver for plasmonic solar cells. By	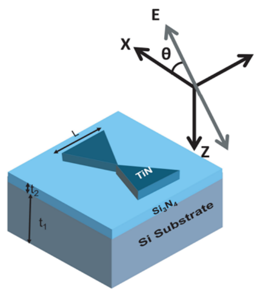	[9]

		plasmonic performance to noble metals (Ag and Au) in photovoltaic applications, with a light absorption efficiency of ~30% and a maximum scattering cross-section of 4.58 Wm^{-2} for bowtie-shaped nanoplates. ● The study identified optimal parameters for TiN nanostructures, including bowtie-shaped designs,	optimizing bowtie-shaped TiN nanostructures through systematic simulations, the study achieved enhanced light absorption (~30%) and scattering (4.58 Wm^{-2}) across visible and infrared wavelengths. This approach not only overcomes the limitations of conventional plasmonic materials but also introduces design strategies—such as polarization-sensitive geometries and dielectric layer tuning—for efficient light trapping in thin-film photovoltaics. The findings provide a scalable, CMOS-compatible solution for next-generation solar energy harvesting.	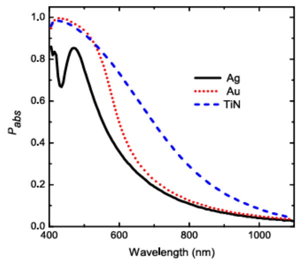	

		thicknesses between 100–200 nm, and a 30 nm Si_3N_4 dielectric layer, which maximized light absorption and scattering. ● TiN nanoparticles enhanced absorption across visible and infrared wavelengths, making them suitable for solar cell applications requiring broadband light manageme			

		nt.			
Simulation study of reducing reflection losses in all-perovskite tandem solar cells through dual serrated structure	2025	● Proposal of the optimization of a dual-interface serrated microstructure to mitigate these optical reflection losses in all-perovskite tandem solar cells ● Expected efficiency boosting of of all-perovskite tandem solar cells to approximately 31.13%, representing a 3.41% increase.	The structural modification reduces the reflection-induced photocurrent density loss from 4.47 to 3.65 mA cm−2. It is expected to boost the efficiency of all-perovskite tandem solar cells to approximately 31.13%, representing a 3.41% increase.	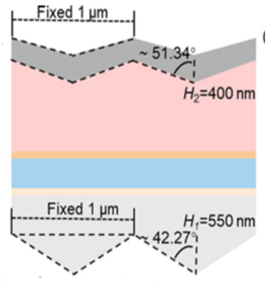 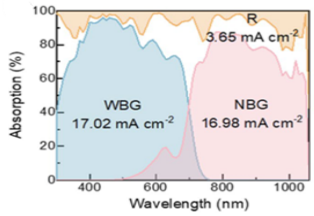	[10]

		• The dual-interface optimization effectively suppresses reflection losses and improves the overall photocurrent of all-perovskite tandem solar cells			

Surface texturing, utilization of back reflectors, and various other approaches have been proposed for enhancing absorption in thin film solar cells [11,12]. Recently, plasmonics has been used for light trapping employing metal nanoparticles [13] and alternative plasmonic materials [14]. Surface plasmons are collective oscillations of the free charges at the metal surface. Metals sustain surface plasmons, either localized in the metal nanoparticles or propagating in the case of planar metal surfaces. By controlling the size and shape of the metallic nanostructures, and the polarization angle of the source, the surface plasmon resonance or plasmon propagation can be tuned. Since the surface plasmon resonance of metal occurs primarily in the visible or the infrared wavelength region, they are of particular interest for photovoltaic applications [15,16]. The development of glass plastic materials based thin film solar cells on the substrate could be an apace growing market [17]. However, these solar cells are affected by some common issues like low efficiency, intense degradation of recombination rate, and less stability. A convenient way to increase the effective path length into the cell is to use surface texturing, which causes the scattering of light into the solar cell over a large angular range [18–20]. The performance of these solar cells can be decreased by the larger surface area due to an increase in minority carrier recombination.

Several solutions for more effective light concentration and trapping have been proposed in recent years to solve these issues, particularly using plasmonic structures made of thin metal films or nanoparticles [21]. They were quite successful at enhancing and redirecting the incident light beam. Plasmonic structures have diverse applications [22], especially in the field of photovoltaics [23–25] where many different technological approaches were proposed to exploit plasmon excitation and light localization for highly efficient solar cells. Many studies were conducted illustrating the coupling of plasmons to optical emitters, plasmon focusing, and hybridized plasmonic modes in nanoscale metal shells [26–29]. Despite all these instigating scopes, until recently little methodical thought has been given to the question of how whole EM spectra can be utilized in a solar cell using plasmon excitation and light localization. To allow near-perfect light absorption and photo carrier collection conventionally, photovoltaic absorbers are required to be "optically thick". To improve the efficiency of solar cells the system must have minority carrier diffusion lengths several times the material thickness for all photo carriers to be collected [30]. There are several ways of reducing the physical thickness of the photovoltaic absorber layers. Among them, plasmonic structures can be utilized in at least three ways while keeping their optical thickness constant. First, metallic nanoparticles have opened the opportunity to be used as sub-wavelength scattering elements to couple and trap freely propagating plane waves from the sun into an absorbing semiconductor thin film, by folding the solar spectra into a thin absorber layer [31,32]. Second, metallic nanoparticles can be used as sub-wavelength antennas in which the plasmonic near-field is coupled to the semiconductor, increasing its effective absorption cross-section [33]. Third, a thin photovoltaic absorber layer can couple solar spectrum into surface plasmon polarization modes supported at the metal/semiconductor interface by a corrugated metallic film on the back surface [34]. Free electrons as plasma in plasmonic materials can support electronic or plasmon over a broad spectrum from infrared to ultra-violet light. As metals have high optical losses, alternative metals with the lowest ohmic losses can be preferable for plasmonic devices. The material library of nanophotonics for a long time has been limited to noble metals such as gold and silver. They are commonly used metals in plasmonic and optical metamaterial devices because of their small ohmic losses or high DC conductivity. However, loss arising from interband transitions occurs when an electron in the valence band in a metal absorbs a photon to jump to the Fermi surface or when an electron near the Fermi surface absorbs a photon to leap to the following unoccupied conduction band causing a high loss in conventional plasmonic materials. Again, the magnitude of the real part of the permittivity is very large in conventional metals. Most importantly, the optical properties of metals cannot be tuned or adjusted easily and they are not cost-effective. The numerous drawbacks of conventional plasmonic materials have motivated researchers to search for alternatives. There have been numerous reports of several alternative materials that can overcome one or more of the drawbacks mentioned above [35–37]. Metal nitrides such as titanium nitride (TiN), zirconium nitride (ZrN), and tantalum nitride (TaN) are notable for carrying metallic properties within the visible and infrared wavelengths [38–40]. These nitrides are non-stoichiometric, interstitial compounds with large free-carrier concentrations. These materials are refractory, stable, and hard. Amazingly, their optical properties are tunable by varying their composition. Moreover, they are compatible with silicon CMOS technology [26,41]. However, metal nitrides offer fabrication and integration advantages which could be useful to overcome the challenges of the metals.The majority of research on plasmonics are based on noble metals. Noble metals have traditionally been treated as most conventional plasmonic material due to their substantially lower loss as a consequence of limited intraband transition (Drude) and interband transition (Lorentz) loss [42]. In addition to these intrinsic properties, their fabrication is compatible with the existing Si-based fabrication industry enabling their ubiquitous presence in plasmon-based devices [43]. However, there are some issues with conventional plasmonic materials which motivated researchers to find a "more convenient" alternative. So far, ultra-thin metal films (UTMF), which support two-dimensional plasmon, got much attention in plasmonic device research for their near-wavelength size and magnetic properties. In actuality, UTMF can be considered as the successor of thin film technology. UTMF has diverse applications, including photovoltaic cells, transparent conductors, and infrared reflectors [44]. However, trapping centers due to the defects, that were introduced during the fabrication process of UTMF, result in a loss in the plasmonic medium [42]. The grain boundary roughness of plasmonic nanoparticles, utilized in solar cells, significantly contributes to the scattering [45].

To overcome these limitations, there is a need to explore materials that are "less lossy" and chemically stable, less prone to surface roughness and have a higher value of real permittivity. Besides, their carrier concentration should be easily tunable, and most importantly, their fabrication process should be compatible with growth techniques. A detailed study by Naik *et al.* illustrated that metal alloys, transparent conducting oxides (TCOs), III-V semiconductors, metal nitrides, and silicides could be used in plasmonic applications [42]. Various approaches have been adopted to obtain noble metal-like plasmonic properties, i.e., negative and low . Transforming metals to a comparatively "less metal" is one of those approaches. Metal silicides and germanides, ceramics such as oxides, carbides, borides and nitrides have negative real permittivity. However, most of these materials do not have sufficiently low imaginary permittivity. These issues prevent the widespread use of ultra-thin films based on alternative plasmonic materials in optical and optoelectronic devices. However, TiN can be considered as a replacement for noble metals because stoichiometric TiN films on sapphire or other transparent substrates show lower imaginary permittivity profiles in visible and near-infrared (NIR) regions than other transitional metal nitrides [46,47]. In short wavelength region, Au suffers from interband transition loss [48]. TiN can be treated as the equivalent of Au with a loss factor of 3 [49]. Maniyara *et al.* reported a copper-seeded deposition technique that enables optical property tuning of noble metal-based ultra-thin film plasmonic devices [50]. The tunability of plasmonic resonance was demonstrated by varying geometric structures as well as external factors. Most recent reports varied external parameters for plasmon tuning, which are difficult to realize. Moreover, most reports were based on gold or similar noble metals. Most of these noble metals are lossy in certain wavelength regions and do not have stoichiometric properties, which is essential for fabricating plasmonic devices. Hence, the need for a less-lossy, easy-to-fabricate, and tunable plasmonic material for ultra-thin films encourages researchers to explore alternative materials. Importantly, easy and fine control of optical properties can be exciting attributes of optoelectronic devices as well as photonic devices. The extensive study on alternative plasmonic material-based nanoparticles is essential to explore their potential to tune optical properties. Although nanoribbon-shaped structures were reported, different unique nanostructures where various plasmonic modes can be confined are yet to be explored.

Chapter 3

Proposed Designs of Bragg Stacks and 2×3 Spherical-Array Structures for Thin-Film Photovoltaic Light-Trapping

3.1 Bragg (Quarter-Wave) Single-Material Stacks

Quarter-wave condition:

A periodic stack of alternating high- and low-index layers produces constructive interference at the design wavelength (λ_0) when each layer has an optical thickness of one quarter wavelength.

Equation:

$d_i = \lambda_0 / (4 \times n_i)$

where d_i is the physical thickness and n_i is the refractive index of the i-th layer. This arrangement produces a photonic stop-band centered near λ_0 and enhances the local electromagnetic field within the stack and the adjacent dielectric spacer.

Material dispersion and loss

Materials are dispersive; for dielectrics ε″≈′≈0 in the NIR, whereas for metals ε″is nonzero and leads to parasitic absorption. Modeling realistic behavior requires causal dispersion models (Drude–Lorentz or measured complex n(ω)n(\omega)n(ω)) plugged into the transfer-matrix or time-domain solver. The balance between useful field trapping and parasitic loss determines whether a dielectric Bragg stack outperforms metallic alternatives.

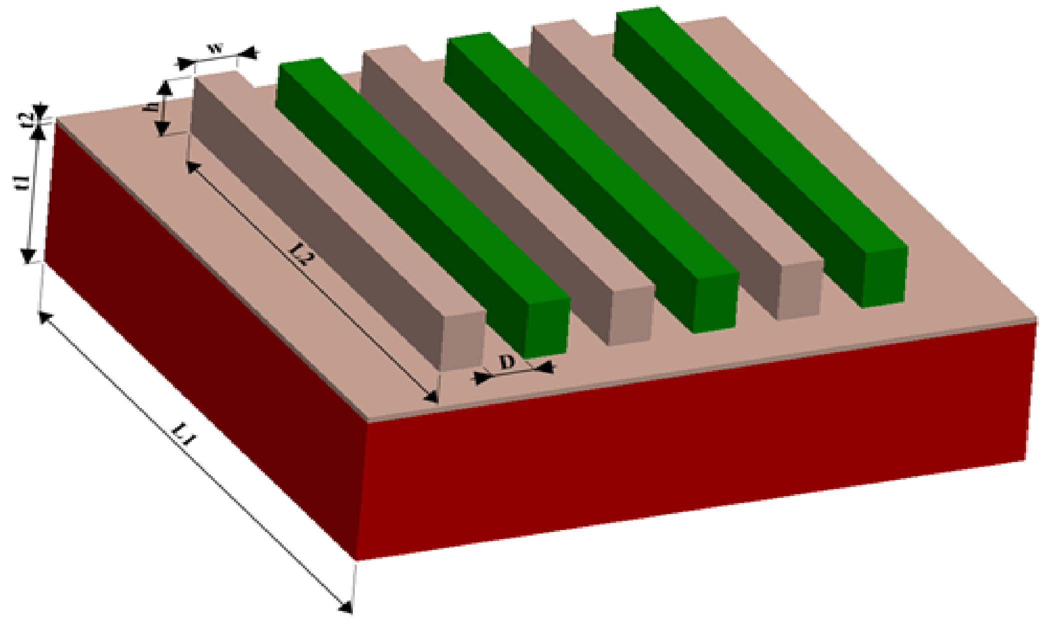

Figure 3.1: Alternating stack design(6 blocks)

Index contrast and reflectivity:

The reflectivity and stop-band width depend on the refractive index contrast (Δn = n_high − n_low) and the number of periods (N). A larger Δn and higher N yield stronger reflection and higher field confinement within the multilayer.

Guided-mode coupling:

A dielectric spacer (for example, Si_3N_4) and a high-index substrate (such as Si) can form a weak waveguiding structure. The evanescent tail of the Bragg-localized field can couple into guided modes at the spacer–substrate interface, increasing the in-plane energy density and enhancing optical absorption in the substrate.

Loss mechanisms:

In dielectric materials where the imaginary part of permittivity (Im ε) ≈ 0, almost all extinction results from coherent reflection or coupling into guided modes. In contrast, metals exhibit nonzero Im ε, causing parasitic absorption and reducing useful optical energy transfer. Therefore, dielectric Bragg stacks are advantageous when low-loss operation and high scattering efficiency are desired.

3.2 Finite 2×3 Spherical Nanoparticle Array

Single-particle scattering:

A spherical nanoparticle with radius of r and permittivity ε_p, embedded in a medium of permittivity ε_m, exhibits a dipolar polarizability given by

$$\alpha = 4\pi \times \varepsilon_0 \times a^3 \times (\varepsilon\_p - \varepsilon\_m) / (\varepsilon\_p + 2\varepsilon\_m)$$

This relation defines how the sphere polarizes under illumination and determines its individual scattering and absorption strengths.

Near-field hybridization:

When multiple particles are positioned at subwavelength separations (edge to edge gap =80 nm gaps for a d1=200 nm lattice pitch), their dipolar modes interact, forming hybridized bonding and antibonding combinations. Bonding modes localize electric fields within the gaps and are typically red-shifted relative to single-particle resonances.

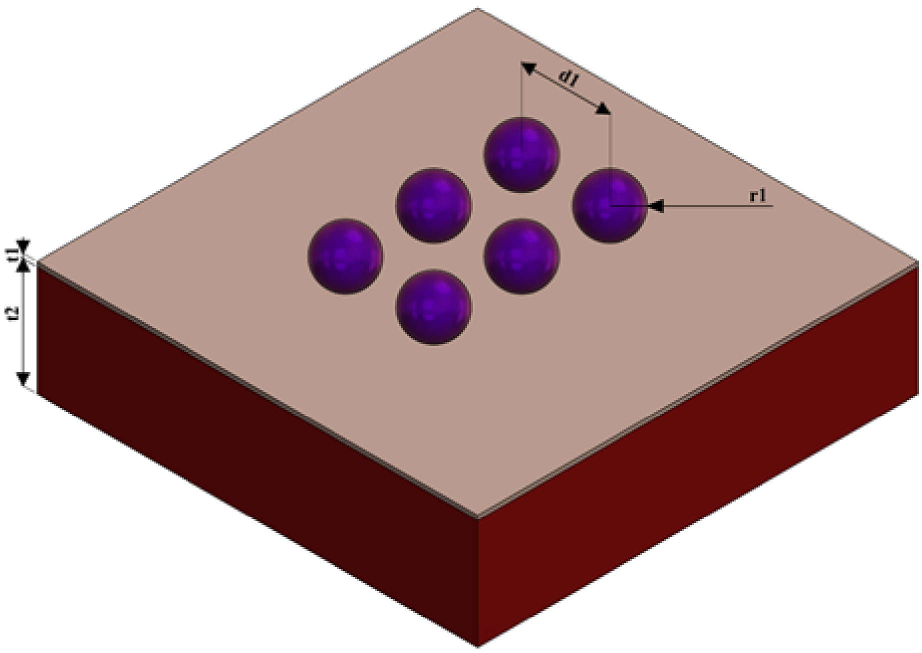

Figure 3.2 : 2x3 Spherical Array

Finite-cluster effects (2×3 array):

A 2×3 rectangular cluster supports strong near-field coupling between adjacent spheres. Central particles experience stronger hybridization (two neighbors), while edge particles have weaker coupling (one neighbor). This nonuniform interaction leads to mixed resonance strengths and multiple peaks in the scattering spectrum—typically a short-wavelength bonding resonance and a longer-wavelength supermode.

Substrate influence and image effects

The proximity of a high-index substrate breaks the cluster symmetry and modifies both radiative damping and near-field coupling (image dipoles and modified Green's tensor). As a result, cluster resonances shift and can gain radiative or guided-mode coupling pathways that are absent in free space. Quantification requires including the substrate Green's function in the CDA or full-wave FDTD, which captures leakage into substrate modes assessed in the Methods.

3.3 Material and Performance Considerations

- **Permittivity role:** The real part of permittivity (Re ε) determines resonance position and field confinement, while the imaginary part (Im ε) dictates absorption loss. Low-loss dielectrics are ideal for maximizing scattering with minimal parasitic heating.

- **Figures of merit:** A common measure of performance is the normalized total efficiency, defined as
  $Q_{\square} = (\sigma_{sca} + \sigma_{abs}) / A_{geom}$
  where σ_{sca} and σ_{abs} are the scattering and absorption cross sections, and A_{geom} is the projected geometrical area of the structure.

- **Design trade-off:** Larger scattering cross sections often accompany higher absorption losses in metals; therefore, the optimal configuration balances field enhancement, material loss, and coupling efficiency into guided substrate modes.

Chapter 4

Methodology

4.1 Method of Simulation

We describe here the experimental-design style and numerical workflow used to evaluate (a) Bragg (alternating-layer) stacks assembled from single chosen material pairs, and (b) finite spherical-array clusters in a 2×3 geometry. All electromagnetic calculations are performed with a finite-difference time-domain (FDTD) solver (Lumerical/FDTD Solutions); the FDTD procedure, post-processing metrics and convergence checks follow standard practice for plasmonic/photonic light-trapping studies.

4.1.1 Bragg (alternating-layer) — single-material cases

We quantify how an N-period quarter-wave stack (alternating high- and low-index films) modifies reflectance, near-field intensity in a buried spacer, and coupling into substrate guided modes at the design wavelength **λ_0 ≈** 900 nm.

• **Geometry & materials** — construct 1D multilayer stacks on a crystalline-Si substrate separated by a thin spacer (Si_3N_4, $t_{□□acer}$ ≈ 20–40 nm). Each layer's physical thickness is set by the quarter-wave condition:

$t = \lambda_0 / (4n)$

(where *n* is that layer's refractive index at λ_0). Typical stacks considered: 3–6 periods of ($n_{□igh}$ / $n_{□ow}$). Evaluate alternative single-material pairings (, TiO_2/SiO_2, Si/SiO_2, metal/dielectric variants) but keep the quarter-wave design methodology consistent across materials.

• **Boundary conditions & excitation** — simulate a stack with a semi-infinite Si substrate (modeled thick enough to absorb transmitted energy) and air superstrate. Use a normally-incident plane-wave source (broadband pulse covering 400–1100 nm or focused 700–1000 nm depending on study). For angular sensitivity, perform additional runs with oblique incidence (s- and p-polarizations).

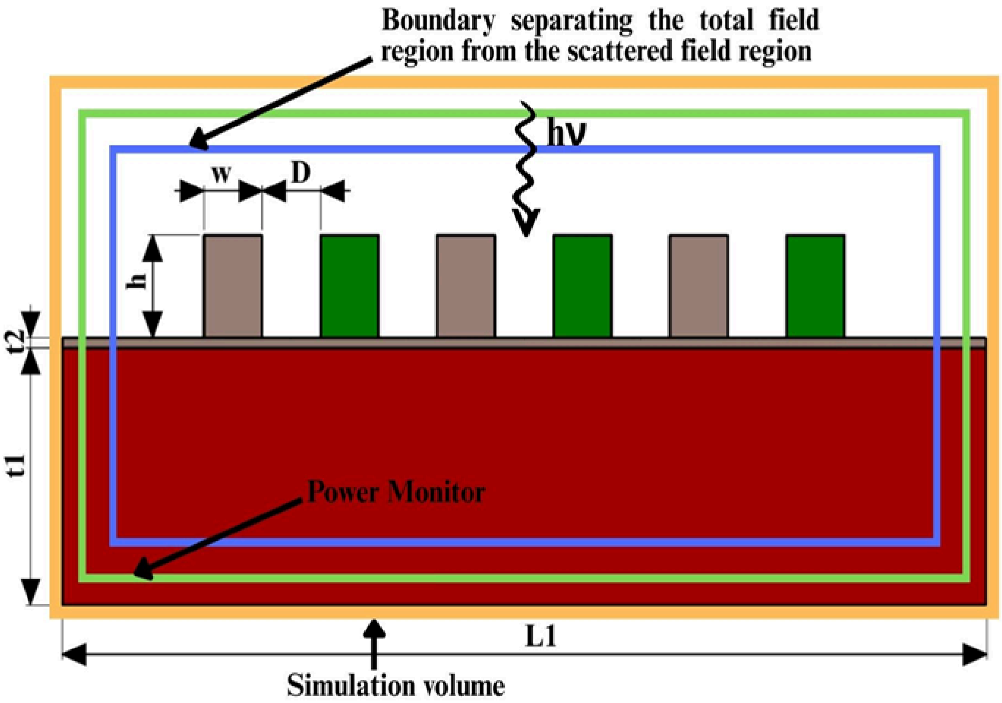

Figure 4.1: Alternating stack design(monitor view)

• **Observables & metrics** — record spectral reflectance, transmittance and absorption in each layer using frequency-domain power monitors; compute field enhancement in the spacer and evaluate guided-mode coupling by placing in-plane monitors and power flux integrals across planes inside the substrate. Normalize results to incident irradiance and extract spectral quantities (reflectance R(λ), absorption A(λ), and the fraction of power coupled into guided in-plane channels).

• **Sweep parameters** — vary number of periods *N*, index contrast (choice of materials), and spacer thickness to map stop-band position, bandwidth, and coupling efficiency. For each material case evaluate parasitic absorption (absorption inside stack materials) versus useful absorption in the Si substrate.

4.1.2 Spherical-array — finite 2×3 cluster (generic procedure)

We evaluate near-field hybridization, spectral positions of bonding/antibonding peaks, and the cluster's normalized extinction (**Q**□) when six spheres (radius *r*, center-to-center pitch Λ) form a 2×3 rectangular cluster above a dielectric spacer on Si. Typical parameter set: *r* = 50–70 nm, Λ = 200 nm (edge-to-edge gaps ≈ 80 nm), spacer t□□$_{acer}$ = 10–30 nm.

• **Geometry & materials** — place six spheres in a planar 2×3 arrangement above the spacer layer; consider several materials (Au, Ag, TiN, ZrN, dielectric Si or TiO_2) using experimentally measured complex permittivities. For finite clusters use a single cluster in a sufficiently large computational domain with absorbing boundaries (PML).

• **Excitation & detection** — illuminate with a linearly polarized plane wave (broadband pulse covering visible–NIR). Use a total-field/scattered-field (TFSF) source to separate incident and scattered fields and place near- and far-field monitors around the cluster to capture scattered power, power into the substrate, and absorption inside each particle. Map the near-field |**E**| distributions in planes that cut through the gaps to visualize hotspot formation and modal hybridization.

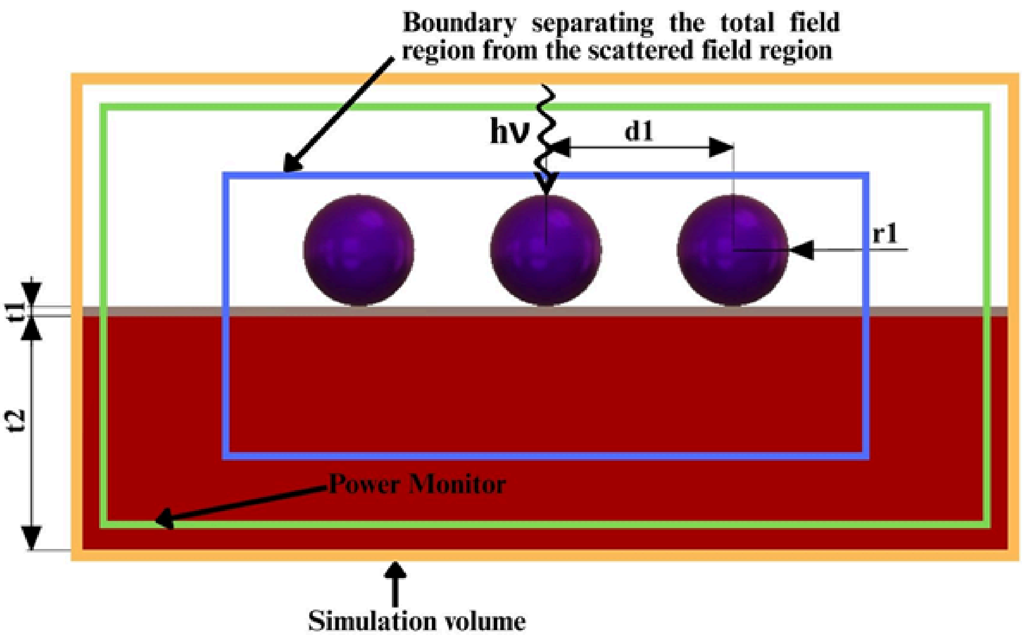

Figure 4.2: 2x3 Spherical Array (monitor -side view)

• **Metrics & data processing** — compute total scattered power P□ via surface integrals of the Poynting vector on an enclosing box, obtain extinction and absorption cross sections by normalizing to incident intensity, and report normalized device metrics (Q□, Q□c, Q_ab) using the same normalization conventions as in established literature. Identify and label spectral features (short-λ bonding peaks, long-λ supermodes) and quantify how peak positions and amplitudes shift with material choice and gap.

• **Parametric sweeps** — vary gap/pitch, sphere radius, material permittivity, and spacer thickness to isolate near-field versus substrate-coupled resonances. For finite clusters, explicitly check end-sphere vs central-sphere contributions by local field integration.

4.1.3 Spherical-array — finite 2×2 cluster

We quantify extreme near-field bonding hybridization, the resulting red-shifted bonding/dimer resonances, and the normalized extinction efficiency (Q_t) for a tightly-coupled 2×2 cluster of spheres placed above a dielectric spacer on Si. Typical parameter set: sphere radius (r = 50)–70 nm, center-to-center pitch Lambda = 200 nm (edge-to-edge gap approx 80 nm), spacer (t= 10–30 nm). Emphasis is on sub-100 nm gaps where gap plasmons / bonding dimers dominate the response.

• **Geometry & materials** — We arrange four identical spheres in a 2×2 square on a planar spacer above crystalline Si. Materials studied include Au, Ag, TiN, ZrN, Sn and high-index dielectrics (Si, TiO_2); use experimentally measured complex permittivities (or fitted Drude–Lorentz models) for each. Simulate a single isolated cluster in a large computational domain with perfectly-matched layers (PML) on all outer faces; exploit any applicable symmetry planes (while noting that symmetry can suppress asymmetric supermodes).

• **Excitation & detection** — We illuminate with a linearly-polarized plane wave (broadband pulse spanning the visible–NIR). Use a total-field / scattered-field (TFSF) source to separate incident and scattered fields. Place an enclosing box of near- and far-field monitors (frequency-domain power monitors and 2D/3D field monitors) around the cluster to capture: (i) scattered power into the air half-space and substrate half-space, (ii) absorption within each sphere and in the spacer/substrate, and (iii) near-field (|E|) maps in planes cutting through the gaps and through the particle centers to visualize hotspot formation and gap localization.

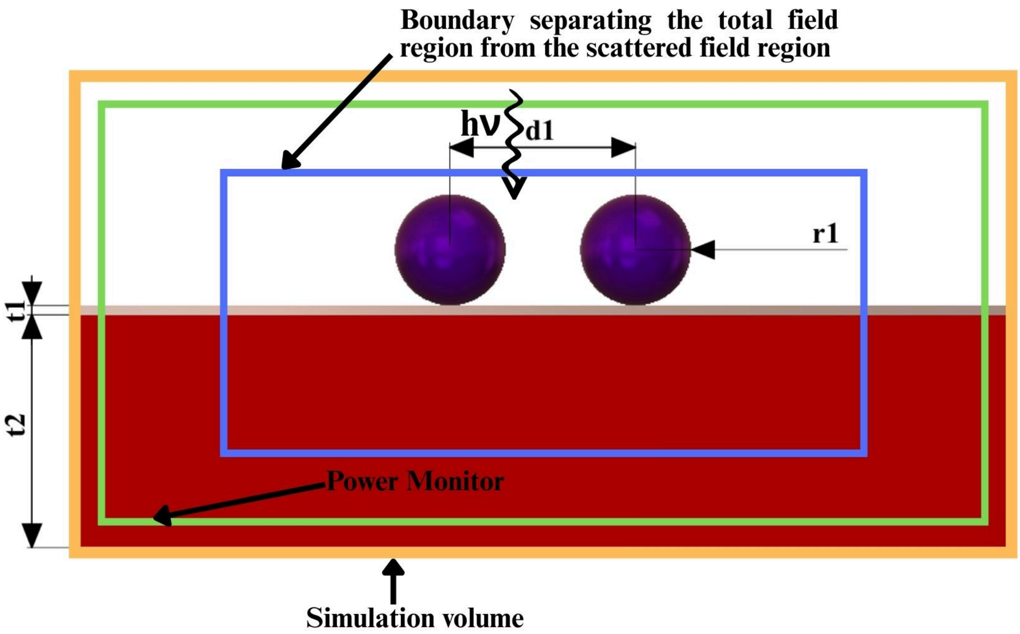

Figure 4.3: 2×2 Spherical Array (monitor-side view)

• **Mesh, domain & convergence** — We apply a non-uniform conformal mesh: coarse in homogeneous air, refined near particle surfaces and across gaps. Typical mesh override: 1–3 nm in gaps for sub-10 nm features (2–5 nm sufficient for 80 nm gaps), 4–8 nm across particle bodies, and larger outside. Ensure mesh convergence by halving the mesh size until spectral peak positions and (Q_t) change by <2–3%. Use PMLs with sufficient thickness (≥0.5–1 λ) and ensure time-step stability is set by the solver.

• **Physics emphasis & expected modes** — the 2×2 geometry strongly favors bonding/dimer modes: adjacent sphere pairs hybridize into intense gap modes that are red-shifted relative to isolated particle LSPRs. Measure the bonding peak (visible band) and any longer-wavelength collective supermodes; quantify the extreme enhancement within the gap and the resulting increase in (sigma)

4.1.4 Spherical-array — finite 4×3 cluster

We evaluate collective near-field and quasi-lattice resonances, modal hybridization across a larger finite lattice, and the normalized extinction per footprint for a 12-sphere array in a 4×3 rectangular layout. Assess how cluster size evolves resonance linewidths, peak amplitudes and substrate coupling relative to smaller clusters (2×3, 2×2). Typical parameters: sphere radius r=50–70 nm, pitch LambdaΛ=200 nm (edge gaps ≈ 80 nm), spacer tspacer=10–40 nm, and spectral window 550–1100 nm.

- **Geometry & materials —** We arrange twelve spheres in a 4×3 planar lattice above a dielectric spacer (Si_3N_4) on Si. Test the same material set (Au, Ag, TiN, ZrN, Sn, Si, TiO_2, Al_2O_3) with measured dispersions. Use a single finite cluster in a computational domain large enough to capture radiative coupling and edge diffraction; apply PML boundary conditions. Optionally simulate a periodic unit cell with Bloch boundaries to compare finite-size behavior with quasi-infinite lattices when appropriate.

- **Excitation & detection —** We illuminate with a linearly polarized broadband plane wave (visible–NIR). Use a TFSF source for scattering separation and position near-field monitors across multiple internal planes (through several gap rows) to capture spatial variation of hotspot strength from center to edge. Use an enclosing Poynting box to compute total scattered power and partition substrate vs air channels; include far-field projections to inspect directionality and beam shaping from the finite lattice.

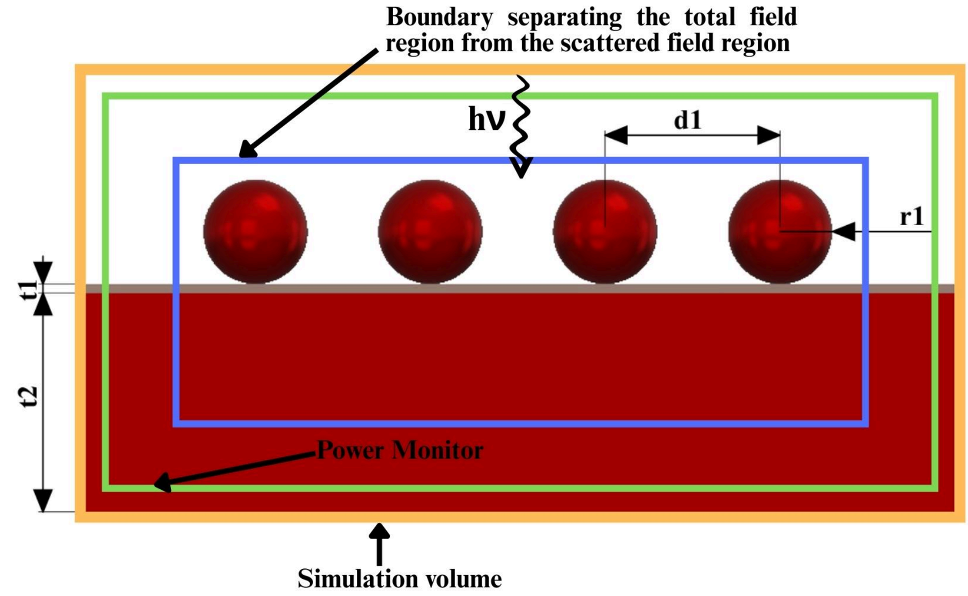

Figure 4.3: 4×3 Spherical Array (monitor -side view)

- **Metrics & data processing** — We extract PsP ,σext, sigma σsc, σab, and normalized metrics Qt, Qsc, Qab as for smaller clusters. Additionally, compute per-particle averaged metrics (divide cluster σ by number of particles) to analyze scaling: how extinction per particle evolves from small clusters to larger finite lattices. Identify lattice-hybrid resonances and quantify linewidth narrowing/broadening with cluster size. Evaluate directionality (angular scattering plots), effective footprint Ageom and edge-to-bulk differences by particle index.
- **Parametric sweeps & convergence** — We sweep pitch LambdaΛ and array aspect ratio (4×3 vs 3×4 or 5×3) to probe anisotropy. Test polarization dependence and oblique incidence. Ensure fine mesh near gaps (2–5 nm) and verify convergence; because the 4×3 geometry supports slower-decaying collective modes, run simulations longer so all resonances decay below the FFT noise floor. Perform energy balance checks and repeat critical runs with refined mesh/time step.

4.1.4 Pyramidal-array — finite 2x2 Array

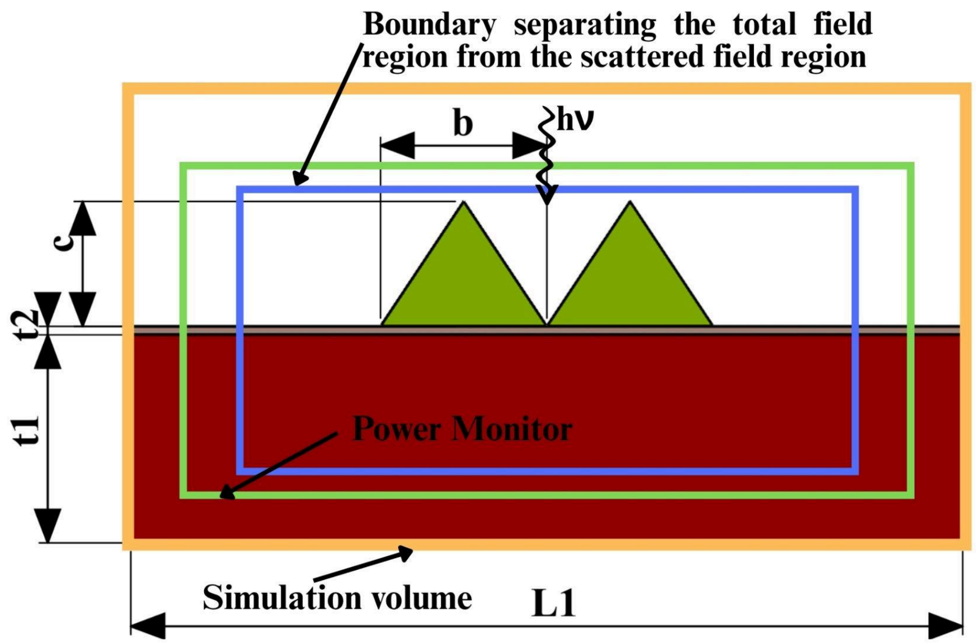

Figure 4.4: 2×2 Pyramidal Array (monitor -side view)

Geometry & Materials —

The 2×2 pyramid array consists of four identical pyramids arranged on a dielectric spacer layer above a silicon substrate. Each pyramid has a base dimension of 200×300 nm^2, a height of 150 nm, and a top width of ~10 nm. The spacer thickness varies between 10–30 nm, optimized for near-field confinement and coupling to the silicon substrate. Materials simulated include Si, TiO_2, TiN, ZrN, Sn, Al_2O_3, Au, and Ag, each modeled using experimentally measured complex permittivities or Drude–Lorentz fitted dispersion data. The computational domain was surrounded by perfectly matched layers (PML) on all boundaries to eliminate reflections, and symmetry boundaries were selectively applied depending on excitation polarization.

Excitation & Detection —

A broadband plane wave source (550–1100 nm) was directed normal to the substrate, linearly polarized along either the x- or y-axis. The total-field/scattered-field (TFSF) formulation was employed to separate incident and scattered fields, with monitors positioned in both near- and far-field zones. The near-field monitors captured electric-field intensity ($|E|^2$) distributions across pyramid apexes and sidewalls to visualize localized hotspots, while far-field monitors recorded scattering, absorption, and total extinction spectra. These measurements were used to compute normalized scattering ($Q_{□ca□}$), absorption ($Q_{ab□}$), and total efficiency ($Q_{□}$) values, benchmarked against the cluster's geometric footprint.

Mesh, Domain & Convergence —

A non-uniform adaptive mesh was implemented to resolve sharp field gradients near pyramid tips and edges. The mesh override was set to 2–3 nm near apex regions and 5–8 nm across sidewalls, with coarser spacing in the air and substrate. The simulation domain extended at least 0.5–1 λ beyond the structure on all sides, ensuring accurate field decay and power capture. Convergence tests were conducted by halving mesh size until the peak wavelength and Qt values varied by less than 2%, confirming numerical stability and accuracy.

Physical Interpretation & Resonance Behavior —

The pyramidal geometry supports hybrid Mie-like resonances and interference-driven cavity modes, producing enhanced electric fields near the apex and along the sloped faces. The strong coupling between individual pyramids in the 2×2 configuration leads to red-shifted bonding modes analogous to plasmonic dimer resonances observed in spherical arrays. The Si and TiO_2 pyramids exhibited dominant dielectric confinement and minimal loss, producing broad, high-Q resonances, while TiN and ZrN demonstrated moderate plasmonic coupling with enhanced thermal stability. Au and Ag, though classically strong plasmonic materials, exhibited weaker overall performance due to damping and substrate losses.

4.2 Lumerical FDTD implementation — detailed procedure and best practices

• **Computational domain & boundaries** —We choose a domain that extends at least 2–3 wavelengths beyond the structure in all directions (unless exploiting symmetry) and terminate with perfectly-matched layers (PML) on all external faces to suppress artificial reflections. When simulating arrays with periodic boundary conditions (not used for finite 2×3 clusters), employ Bloch/periodic boundaries with an appropriate phase shift for oblique incidence.

• **Mesh strategy & convergence** — use a non-uniform mesh: coarse in homogeneous air, progressively refined near material interfaces and subwavelength gaps. Apply a dense conformal mesh override around metals/dielectrics and inside gaps (typical mesh step 2–5 nm near nanoparticles; 1–2 nm for sub-10 nm gaps), and ensure that results are mesh-converged (verify by halving the mesh size until peak spectral shifts and extracted cross-sections change by <2–3%). Use the default Courant-stability time step or let the solver compute **Δt** from mesh.

• **Source & polarization** — implement a TFSF plane-wave pulsed source when extracting scattering/absorption for isolated particles/clusters to numerically separate incident and scattered fields. For stack reflectance/transmittance use a total plane-wave source with monitors above and below the stack. Perform polarization sweeps where appropriate.

• **Monitors & diagnostics** — place frequency-domain field and power monitors:
(i) near-field E/H monitors (2D planes and 3D volumes) for spatial mode maps and LDOS estimates;
(ii) surface monitors (closed box) for total scattered power $P_{□}$;
(iii) transmission/reflection monitors for R/T spectra; and
(iv) volume monitors inside particles and substrate to compute dissipated power (absorption).
Use mode projection monitors if you need to quantify power coupled into specific guided modes.

• **Material modeling** — import complex permittivity data (n & k or ε(ω)) for all materials from handbooks or ellipsometry (Johnson–Christy for Au/Ag, experimentally measured TiN/ZrN datasets for nitrides, and vendor/ellipsometric data for dielectrics). Fit dispersive models (Drude–Lorentz or multi-pole fits) to measured data within Lumerical to ensure causal dispersion and stable time-domain integration.

• **Simulation time & Fourier analysis** — run for sufficient time to allow the broadband pulse to decay below a prescribed threshold in the monitors (e.g., fields $<10^{-6}$ of peak). Apply Fourier transforms to the recorded time-domain fields to produce spectral quantities: **E(ω)**, **H(ω)**, Poynting flux **S(ω)**, and derived cross sections (following the algebra shown in common references). Use windowing where necessary to reduce spectral ringing.

• **Post-processing** — compute spectral cross sections by normalizing measured powers to incident intensity (units: m^2 or W/m^2 depending on normalization); calculate normalized
$Q_{□} = (\sigma_{□} c_{a}{□} + \sigma_{a} b{□}) / A_{geom}$

as needed for device-level comparison. Visualize near-field maps at resonance wavelengths to identify bonding/antibonding character and hotspot locations.

4.3 Lumerical FDTD implementation Computational Strategies and Equations

The finite-difference time-domain (FDTD) method was used to numerically solve Maxwell's curl equations in both space and time domains while enabling full-wave modeling of scattering, interference, and absorption phenomena.

The simulation domain used in the designed models measured 1.2 µm × 1.2 µm × 1.25 µm, with perfectly matched layer (PML) boundaries applied on all sides to eliminate spurious reflections. A non-uniform mesh size of 4 nm was applied around the nanoparticles to accurately capture local near-field variations.

A total-field/scattered-field (TFSF) plane-wave source was incident along the **+z** direction and polarized in the plane of the structure to provide uniform illumination. By isolating the scattered fields through subtraction of the known incident field from the total field, accurate computation of scattering was achieved using the TFSF method.

The illumination covered wavelengths ranging from 550–1100 nm, corresponding to the high-irradiance region of the AM 1.5 solar spectrum.

The time-domain electric fields were converted to the frequency domain using the Fourier transform:

$$E(\omega) = \int_0^{T} f\, E(t) \cdot e^{(i\omega t)}\, dt$$

The frequency-domain Poynting vector was then computed as:

$$S(\omega) = \mathrm{Re}\left[(1/2) \cdot E(\omega) \times H^*(\omega) \right]$$

This frequency-domain power density was integrated over monitor planes to compute directional scattering. For example, scattered power along the +x and +y directions was obtained as:

$$P_1 = \int(y_{min} \rightarrow y_{max}) \int(z_{min} \rightarrow z_{max})\, S_x(y, z, \omega)\, dz\, dy$$

$P_2 = \int(x_{min} \rightarrow x_{max}) \int(z_{min} \rightarrow z_{max}) S_\gamma(x, z, \omega)\, dz\, dx$

By summing the contributions from all six monitors enclosing the TFSF region, the total scattered power was determined:

$P□ = P_1 + P_2 + P_3 + P_4 + P_5 + P_6$

The total scattered power was then used to compute the total scattering cross-section and absorption cross-section using:

$Q□(\omega) = P□(\omega) / I(\omega)$

$Q_a b = P_a b□ / (I(\omega) \cdot A_i□□_u□)$

where $I(\omega)$ is the incident intensity and $A_i□□_u□$ is the illuminated area.

The fraction of scattered power directed into the substrate, indicating how efficiently scattered light couples into the photovoltaic absorber, was calculated as:

$f□_u\_b = P□c,Si / (P□c,air + P□c,Si)$

For comparison across geometries, the extinction efficiency was normalized to the particle's geometric cross-section:

$Q□ = \sigma_{ex}□ / A\_g_{eo}□$

Chapter 5

Result Discussion and Analysis

5.1 . Bragg Stack Design (Alternating Layered Structure)

The optical behavior of nanostructured materials depends strongly on their geometry, layer composition, and the way light interacts with them. This chapter presents the comparative optical performance of two key resonator types — the Bragg stack design (alternating layered structure) and the spherical array design (plasmonic particle arrangement).

The Bragg stack relies on constructive interference between multiple alternating layers to reflect and trap specific wavelengths of light efficiently. The spherical array, on the other hand, uses plasmonic coupling between closely spaced nanospheres to amplify local electromagnetic fields.

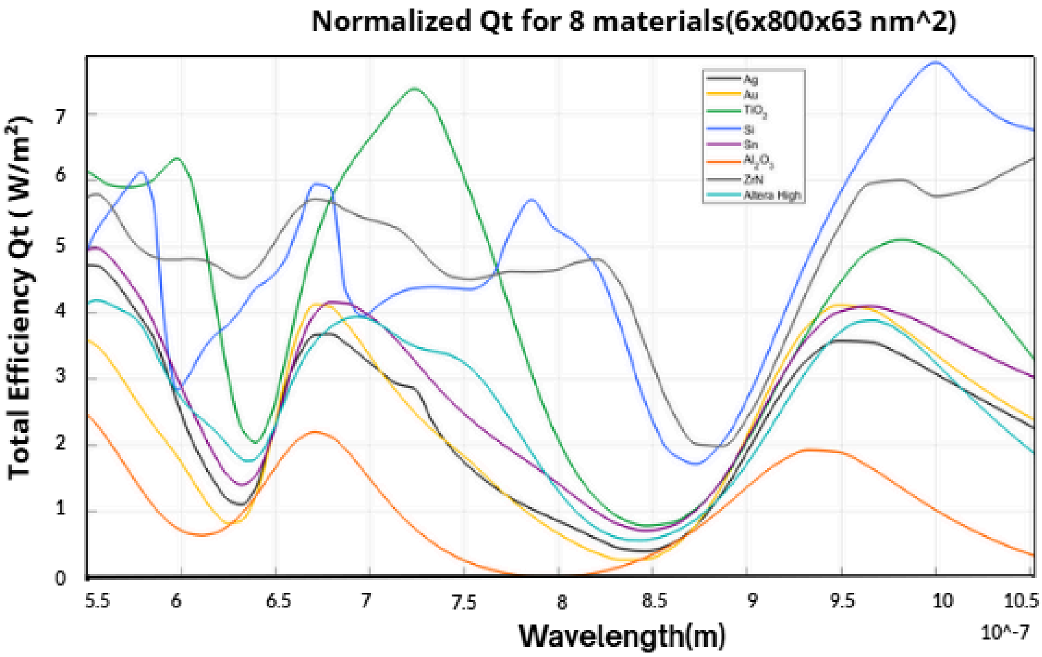

Figure 5.1: Alternating Bragg resonator output

Both configurations are evaluated using normalized total efficiency (Qt) as a performance indicator. The analysis covers peak wavelengths, material performance, design-dependent variation, and comparative observations between metallic, dielectric, and hybrid structures.

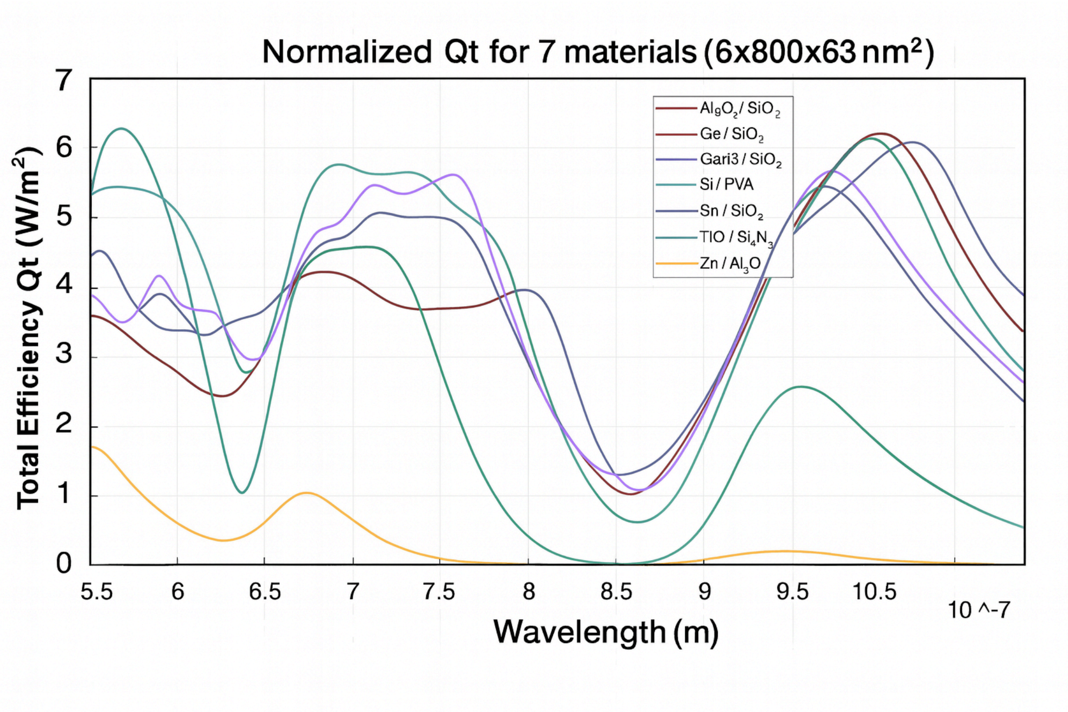

Figure 5.2: Alternating Bragg resonator output with Material pair

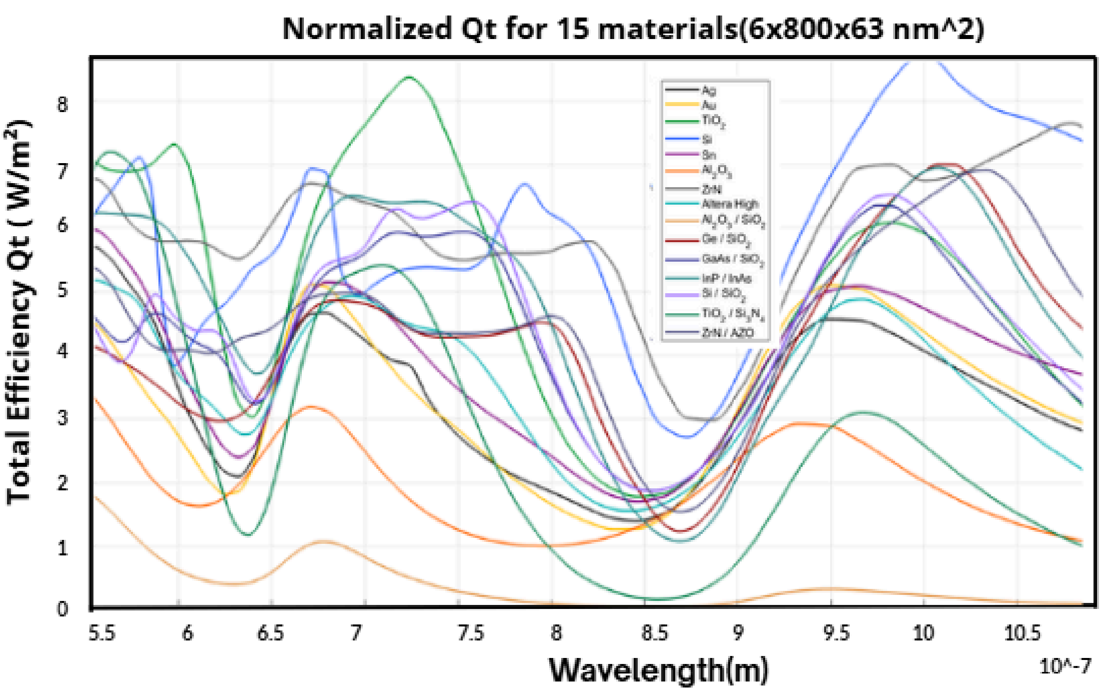

Figure 5.3: Alternating Bragg resonator output with a single material and Material pair

5.1.1 Overview of the Bragg Structure

The Bragg stack, also known as a one-dimensional photonic crystal, consists of alternating layers of high- and low-index materials arranged periodically. When light strikes this structure, part of it reflects at each interface, and these reflected waves can combine in phase if the layer thickness satisfies the quarter-wave condition.

This in-phase reinforcement produces constructive interference, leading to strong reflection and minimal transmission at specific wavelengths, called stop bands. The design is highly effective in light management applications, such as solar reflectors, photonic mirrors, and multilayer optical coatings.

Figures 5.1-5.3illustrate the performance of single-material stacks, alternating pairs, and their combined configurations.

5.1.2 Material-Specific Performance (From Figure 5.1)

The single-material Bragg configuration reveals that the dielectric materials — particularly silicon (Si) and titanium dioxide (TiO_2) — produce the highest reflection and energy confinement.

- Silicon (Si) achieves the strongest efficiency, with a maximum Qt ≈ 8.5 at a wavelength of 9.9×10^{-7} m. Its high refractive index and low absorption allow strong optical confinement through internal reflection.

- Titanium dioxide (TiO_2) shows a similar Qt ≈ 8.5 at 7.3×10^{-7} m, performing equally well but at a shorter wavelength due to its higher permittivity. TiO_2's low loss (nearly zero imaginary permittivity) minimizes heat generation, making it ideal for optical coatings.

- Zirconium nitride (ZrN) ranks next with Qt ≈ 7.0 at 9.6×10^{-7} m, showing excellent NIR performance.

- Gold (Au) and tin (Sn) both yield moderate values (Qt ≈ 5.2) near 6.6–6.7 $\times 10^{-7}$ m, while silver (Ag) is slightly lower (Qt ≈ 4.8), limited by oxidation and damping losses.

- Aluminum oxide (Al_2O_3) produces the weakest response (Qt ≈ 3.2 at 6.7×10^{-7} m) due to its low refractive index and minimal light interaction.

In summary, Si and TiO_2 dominate with high reflection and minimal thermal loss, followed by ZrN, while metallic materials and Al_2O_3 remain less effective.

5.1.3 Material Pair Performance (From Figure 2 —Figure5.2)

When materials are paired in alternating bilayers, their optical response depends on refractive index contrast — the degree of light bending at the interface.

- Low-contrast pair (Al_2O_3–SiO_2): Exhibits a stable but moderate Qt ≈ 6.8×10^{-7} m, maintaining smooth interference.

- High-contrast pairs:

    - Ge–SiO_2 achieves Qt ≈ 7.0 at 1.02×10^{-6} m, creating a broad stop-band.

    - GaAs–SiO_2 peaks at Qt ≈ 6.2 at 9.7×10^{-7} m, limited by absorption in GaAs.

- Medium-contrast pairs:

    - InP–InAs shows Qt ≈ 6.99 at 1.0×10^{-6} m, optimized for the mid-IR range.

    - TiO_2–Si_3N_4 performs best in this group with Qt ≈ 7.2 at 5.6×10^{-7} m, benefiting from negligible losses (Im ε ≈ 0) and strong coupling back into silicon.

- High-contrast pair (Si–SiO_2): Displays Qt ≈ 6.5 at 9.75×10^{-7} m, with very strong reflection but slightly harder tuning due to the wide refractive index gap.

Summary: The TiO_2–Si_3N_4 pair provides the best balance of low loss and stability, while Ge–SiO_2 is best for broader reflection bands.

5.1.4 Comparative Design Behavior (Design 1 vs. Design 2)

The Bragg stack's spectral performance shifts with layer arrangement.

- In **Design 1 (conventional alternating stack)**, the primary peaks occur at 600 nm and 725 nm.

- In **Design 2 (mixed alternation)**, the peaks shift to **570 nm** and **1020 nm** as the structure alternates high–high or low–low refractive indices.

This shift results from changes in the optical path length and periodicity, modifying how waves interfere inside the stack.
Design 1 offers sharp, narrow peaks, while Design 2 produces a broader spectral response and more flexible tunability.

5.1.5 Overall Alternating Stack Analysis (From Figure 3)

Fifteen configurations were simulated, including metals (Ag, Au), nitrides (TiN, ZrN), oxides (TiO_2, Al_2O_3), semiconductors (Si, Ge, GaAs, InP/InAs), and hybrids (TiO_2/Si_3N_4, Si/SiO_2, ZrN/AZO).Each used six 800 nm × 63 nm layers on 30 nm Si_3N_4/Si. Three optical regimes were identified:

a) Visible Bonding Regime (550–700 nm)

Top performers: TiO_2 (Qt ≈ 7.5 at 680 nm), Si (Qt ≈ 7.0 at 660 nm), ZrN/AZO (Qt ≈ 7.0 at 620 nm). These materials exhibit strong Mie-type resonances and bonding-dimer modes, enhancing field confinement. Metals (Au, Ag) show Qt ≈ 4.7–5.3, with Ag peaking near 550–600 nm, slightly outperforming Au.

b) Mid-IR Quasi-Lattice Regime (700–850 nm).Key materials: TiO_2/Si_3N_4 (Qt ≈ 6.8 at 780 nm), InP/InAs (Qt ≈ 6.5 at 800 nm), Si (Qt ≈ 6.2 at 760 nm).Alternating layers act as 1D optical gratings, forming quasi-lattice resonances that enhance reflection. Metals show broader, lower peaks (Qt ≈ 4.0–4.2) due to ohmic damping.

c) NIR Bragg-Stop Regime (900–1050 nm)

Dominant materials: Si/SiO_2 (Qt ≈ 9.0 at 950 nm), Ge/SiO_2 (Qt ≈ 8.7 at 940 nm), InP/InAs (Qt ≈ 8.0 at 920 nm), ZrN (Qt ≈ 7.5 at 960 nm).High-index contrasts form quarter-wave Bragg reflectors, creating wide stop-bands (~100 nm). Metals (Au/Ag) fall to Qt ≈ 4.5–5.0, since their plasmonic resonances weaken beyond the visible spectrum.

Conclusion:

Bragg stacks with dielectric and hybrid layers outperform metallic systems, achieving strong constructive interference and minimal thermal loss across all spectral regions.

5.2 Spherical Array Design

The spherical array design consists of periodically arranged nanospheres on a substrate. When light interacts with these spheres, it excites surface plasmon resonances — collective oscillations of electrons on the sphere surfaces. These oscillations can couple between neighboring spheres if they are closely spaced, producing bonding supermodes that amplify the scattered field.

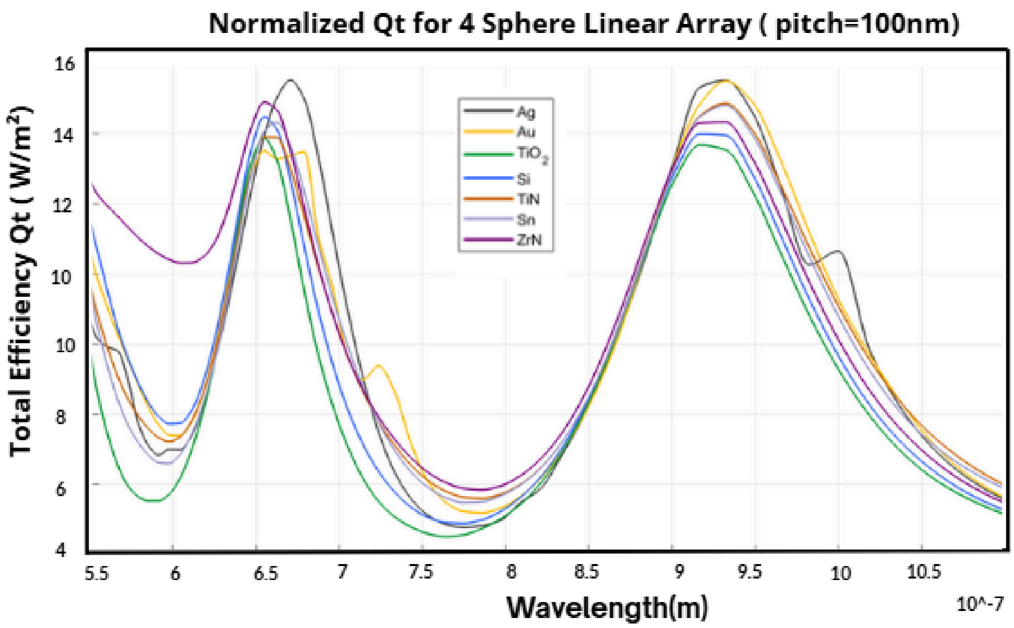

Figure 5.4: 2x2 Spherical array output

The optical response depends on both sphere material and inter-sphere spacing. Tighter packing leads to stronger plasmonic coupling and higher total efficiency (Qt).

Three configurations were analyzed: 2×2, 2×3, representing increasing spatial complexity.

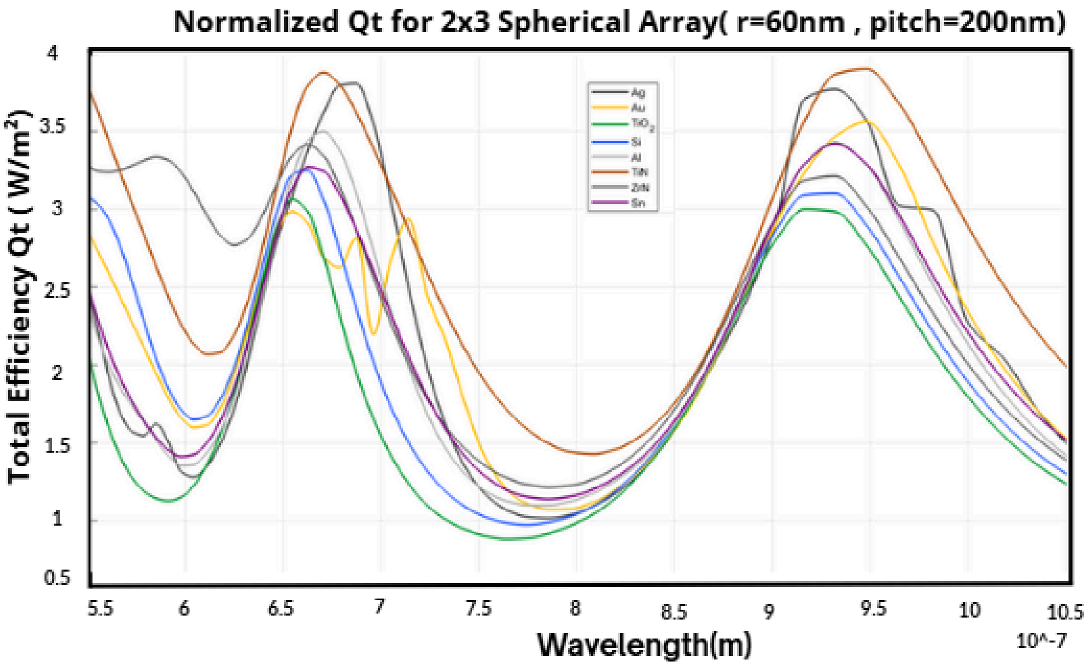

Figure 5.5: 2x3 Spherical array output

5.2.1:Optical Performance of Spherical Arrays

(a) 2×2 Array

In this compact arrangement, Ag and Au perform exceptionally well, reaching Qt ≈ 17–18 at wavelengths near 675 nm and 950 nm. These high values arise from strong near-field coupling across narrow 80 nm gaps, creating intense *bonding dimer supermodes*.

TiN and ZrN follow closely (Qt ≈ 12–14), offering more stable plasmonic responses with excellent thermal and chemical durability. Tin (Sn) peaks near Qt ≈ 15–16, but damping effects cause energy loss as heat, broadening its resonance.

(b) 2×3 Array

As spacing increases, coupling weakens. The top performer here is TiN, with Qt ≈ 4.4 at 920 nm. Gold and silver follow with Qt ≈ 3.8–4.0, while ZrN (3.6) and Sn (2.8) show broader peaks.

Dielectric materials such as Si, TiO_2, and Al_2O_3 remain weak (Qt ≤ 2.5) due to a lack of free electrons, preventing plasmonic resonance.

5.2.2 Comparative Discussion

The 2×2 array consistently yields the strongest results due to its compact geometry, allowing localized fields to merge into coherent resonant modes. As the array expands (2×3), plasmonic coupling decreases, and energy confinement weakens.Among materials, Ag and Au provide the highest peaks but suffer from thermal instability and oxidation.

TiN emerges as the most reliable non-noble-metal option, maintaining reasonable efficiency with minimal degradation — a strong candidate for practical plasmonic devices that balance performance and durability.

5.3:Optical Performance of 2x2 Pyramid Arrays

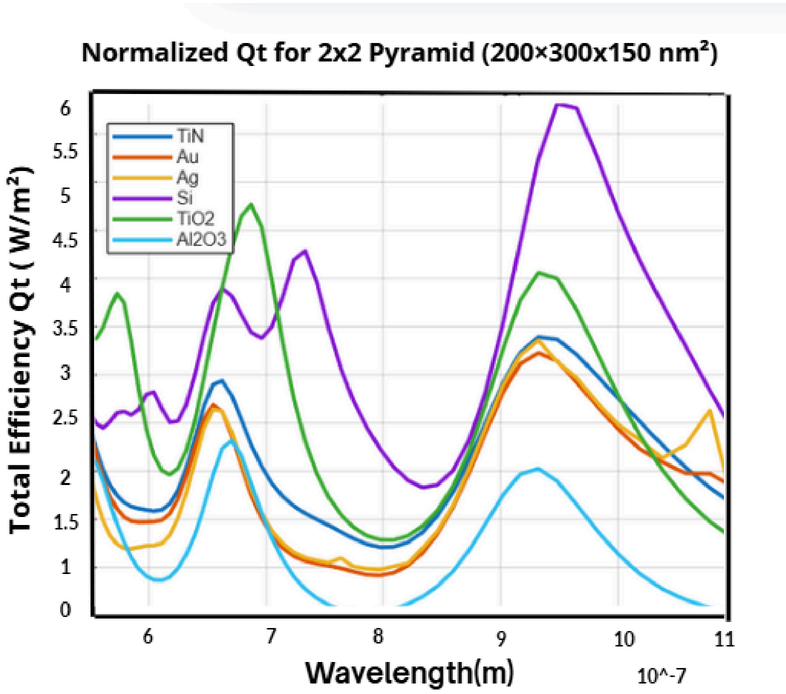

Figure 5.6: 2x2 Pyramidal array output

In the 2×2 pyramid structure (200×300×150 nm²), the maximum normalized total efficiency (Qt ≈ 5.9 W/m²) is achieved by silicon (Si) at around 950 nm, marking the strongest overall response among all tested materials. This broad and intense peak originates from Mie-like dielectric resonances and cavity interference effects within the pyramidal geometry, where constructive internal reflections amplify the local field. Titanium dioxide (TiO_2) shows the second-highest efficiency, peaking near 930 nm with Qt ≈ 4.2 W/m², attributed to its high permittivity and low-loss dielectric scattering that enhance light trapping across the visible–NIR range. Together, Si and TiO_2 dominate the spectrum, demonstrating that dielectric confinement and interference govern the optical enhancement in this configuration.

Among metals, titanium nitride (TiN) reaches a moderate maximum of Qt ≈ 2.8 W/m² near 900 nm, providing a broad plasmonic response with good thermal and chemical stability. Gold (Au) exhibits a slightly lower peak (~2.5 W/m² at ~850 nm**)**, limited by substrate damping, while silver (Ag), though theoretically the best plasmonic metal, only reaches ~2.2 W/m² due to oxidation and poor mode coupling with the substrate. Aluminum oxide (Al_2O_3) remains nearly flat throughout, with Qt < 1.8 W/m², confirming its weak light–matter interaction. Overall, Si (5.6 W/m² at 950 nm) stands out as the top performer, followed by TiO_2 (4.2 W/m² at 930 nm)—clearly outperforming metallic counterparts through low-loss dielectric enhancement and geometry-driven field amplification.

5.4 Summary

This chapter demonstrates that both Bragg stacks and spherical arrays achieve high optical performance through different physical mechanisms:

- Bragg stacks exploit *interference and layer contrast*, favoring dielectrics like TiO_2 and Si for loss-free light reflection.

- Spherical arrays rely on *plasmonic resonance and coupling*, favoring metals like Ag, Au, and TiN for field enhancement.
- Silicon (Si) showed the best performance due to its strong dielectric confinement and constructive interference, while TiO_2 followed closely because of its high permittivity and low optical loss, both outperforming metals in light trapping efficiency.

Together, these results provide a comprehensive understanding of how geometry, material selection, and spectral regime govern the optical behavior of nanoscale resonators. The findings offer valuable insight for designing next-generation photonic coatings, plasmonic sensors, and nanostructured solar absorbers.

Chapter 6

Fabrication process and experimental setup

6.1 Introduction

This chapter outlines the computational and experimental approaches used to investigate the optical performance of Bragg resonator stacks and spherical array nanostructures. The study combines electromagnetic simulations with detailed fabrication pathways to demonstrate how theoretical predictions can be translated into realizable nanoscale devices.

Both designs were modeled using finite-difference time-domain (FDTD) simulations to capture their electromagnetic field distributions and resonance characteristics. The simulation setup was complemented by a nanofabrication protocol developed to create experimental prototypes compatible with thin-film photovoltaic applications.

6.2 Numerical Simulation Framework

The simulations were performed within a three-dimensional computational domain measuring approximately 1.2 µm × 1.2 µm × 1.25 µm, enclosed by perfectly matched layers (PML) to eliminate artificial reflections. The mesh was refined to a spatial resolution of 4 nm around nanostructured regions to accurately resolve near-field effects.

A total-field scattered-field (TFSF) plane-wave source was incident along the *z*-axis, and its polarization was varied from 0° to 90° to examine anisotropic scattering responses. The wavelength sweep ranged from 550 nm to 1100 nm, encompassing the key portion of the AM1.5 solar spectrum.

Both isolated nanoparticles and collective arrays were studied to capture individual and coupled optical behavior. These included Bragg-type layered stacks, periodic nanoparticle gratings, and dense spherical arrays. Materials tested were TiN, ZrN, Sn, TiO_2, and Al_2O_3, benchmarked against Au and Ag for comparison.

Near-field monitors were used to map the electric-field intensity along the *xy*, *yz*, and *zx* planes, while far-field monitors recorded scattering spectra along ±*x*, ±*y*, and ±*z* directions.
The main optical quantities of interest were:

- Total scattering efficiency (Q□) – a measure of total scattered energy relative to incident flux.

- Absorption efficiency (Q_ab) – quantifying the fraction of absorbed light.

Time-domain signals were converted to the frequency domain through Fourier transformation, allowing direct comparison of spectral peaks and absorption enhancements across materials and geometries. Optimization procedures were applied to determine ideal layer thicknesses, periodicities, and particle diameters for maximum light-trapping efficiency.

6.3 Experimental Setup for Bragg and Spherical Systems

To address structural differences, the computational and fabrication setups for the Bragg resonator and Spherical array systems were treated separately.

6.3.1 Bragg Stack Resonator Setup

For the Bragg configuration, the simulation domain represented a periodic stack composed of alternating high- and low-index layers on a silicon substrate with a Si_3N_4 spacer. Each layer followed the quarter-wave optical thickness condition to maximize constructive interference.

Boundary conditions were set as periodic in the x–y directions and PML along z, enabling the capture of multiple reflections without edge artifacts. The incident plane wave illuminated the structure normally along *z*, covering the wavelength range of 550–1050 nm.

Material permittivities were imported from experimentally measured refractive index data. The FDTD monitors captured the reflectance (R), transmittance (T), and absorption (A = 1 – R – T), from which Qt was extracted. Layer thickness, material contrast, and sequence (e.g., Si–SiO_2, TiO_2–Si_3N_4) were systematically varied to evaluate their effect on resonance wavelength and field confinement.

6.3.2 Spherical Array Resonator Setup

For the spherical array, the computational cell consisted of periodically arranged nanospheres (2×2, 2×3, 4×3 configurations) placed above a Si_3N_4 spacer layer on silicon. Each sphere had a radius of approximately 60 nm, with inter-sphere spacing tuned from 80 nm to 200 nm to explore different coupling strengths.

The TFSF source was polarized along the *x*-axis to excite surface plasmon modes, and angular far-field monitors captured directional scattering patterns. Both individual spheres and close-packed arrays were tested to quantify the transition from isolated resonance to collective plasmonic coupling.

Spectral response, electric-field maps, and Qt distributions were analyzed to determine how geometry, spacing, and material type influence resonance sharpness and overall optical efficiency.

6.4 Fabrication Methodology

The fabrication workflow for both designs was developed to align with simulation parameters and ensure reproducibility. High-purity materials and thin-film techniques were employed to achieve nanoscale precision in geometry and surface uniformity.

6.4.1 Substrate Preparation

For both systems, crystalline silicon (Si) wafers served as the base substrate due to their optical compatibility with solar and photonic applications. A Si_3N_4 spacer layer (10–30 nm thick) was deposited using plasma-enhanced chemical vapor deposition (PECVD) to provide passivation and control near-field coupling between the nanostructures and the silicon surface. The wafers were cleaned ultrasonically in acetone, isopropanol, and deionized water, followed by drying under nitrogen flow.

6.4.2 Material Deposition

Candidate materials — TiN, ZrN, Sn, TiO_2, and Al_2O_3 — were deposited using the following techniques:

- **Nitrides (TiN, ZrN):** prepared by reactive DC magnetron sputtering in an Ar/N_2 plasma. Gas ratios and deposition power were optimized to tune stoichiometry and optical properties.

- **Oxides (TiO_2, Al_2O_3):** produced via sol-gel spin coating or atomic layer deposition (ALD), followed by annealing at 400–600 °C to achieve the desired crystalline phase.

- **Metallic films (Sn, Au, Ag):** deposited through e-beam evaporation under high vacuum for benchmark comparison.

6.5 Fabrication Process for Bragg Resonator Arrays

The Bragg stack was fabricated as a multilayer thin-film system designed for optical interference enhancement.

1. **Layer Deposition:**
   Alternating high- and low-index layers (e.g., TiO_2–Si_3N_4 or Si–SiO_2) were sequentially deposited on the Si substrate. Layer thicknesses were controlled by deposition time to maintain quarter-wave optical thickness at the target wavelength.

2. **Annealing:**
   Each dielectric layer was thermally treated (450–500 °C) to improve film density and refractive index stability.

3. **Pattern Definition (if periodic gratings required)**:
   For Bragg resonators coupled with nanoparticle arrays, electron-beam lithography (EBL) or nanoimprint lithography (NIL) was used to define periodic surface gratings corresponding to simulation parameters.

4. **Etching and Lift-Off:**
   Reactive ion etching (RIE) refined the pattern edges, while lift-off in acetone removed undesired film regions, leaving precise periodic structures.

5. **Encapsulation:**
   A thin anti-reflection coating (Al_2O_3 or Si_3N_4, ≈ 10 nm) was applied to prevent oxidation and surface contamination.

6. **Integration:**
   The completed Bragg multilayer was integrated with thin-film photovoltaic or photonic test platforms for optical characterization.

6.6 Fabrication Process for Spherical Array Structures

The fabrication of spherical nanostructures required a combination of top-down lithography and bottom-up pattern transfer techniques to replicate the array geometry observed in simulation.

1. **Template Definition:**
   Periodic nanohole templates were defined on a resist-coated substrate using EBL or NIL. The pattern pitch matched the simulated inter-particle spacing (80–200 nm).

2. **Material Deposition:**
   Target plasmonic materials (TiN, ZrN, Sn, Au, Ag) were deposited by sputtering or e-beam evaporation. For TiN and ZrN, reactive sputtering conditions were precisely controlled to achieve smooth, stoichiometric films.

3. **Sphere Formation:**
   The lift-off process produced dome-like or hemispherical nanoparticles, which were then reshaped into spheres through thermal reflow or ion-beam rounding at controlled temperature (≈ 400–450 °C).

4. **Etching and Surface Cleaning:**
   Reactive ion etching (RIE) was used to isolate spheres and tune their height, ensuring well-defined inter-sphere gaps.

5. **Protective Overlayer:**
   A thin dielectric capping layer (Al_2O_3 or Si_3N_4) was deposited for environmental stability and to prevent oxidation of metallic nanoparticles.

6. **Device Integration:**
   The spherical arrays were transferred onto test cells for optical measurements and compared with simulation data to validate resonance shifts and scattering strength.

6.8 **Fabrication Process for 2x2 Pyramid Array:**

Fabrication Process

The pyramidal arrays were fabricated using nanosphere lithography (NSL) to replicate the design demonstrated in TiN plasmonic studies [14]. Pre-patterned ITO-coated soda-lime glass substrates were sequentially cleaned in 2 % Hellmanex III, acetone, methanol, and isopropanol, followed by nitrogen drying. Monolayers of 200 nm and 500 nm polystyrene (PS) nanospheres were self-assembled at the air-water interface and transferred onto UV-ozone-treated substrates to form a hexagonally close-packed mask. Reactive DC/RF magnetron sputtering of TiN or ZrN in Ar/N_2 atmosphere (substrate 200–600 °C, optimized N_2 partial pressure ≈ 15–25 %) deposited the plasmonic film. The sphere mask was removed by gentle sonication, leaving a **2×2 pyramid array** with base ≈ 300 × 200 nm, top ≈ 10 × 10 nm, and height ≈ 110 nm. A 30 nm Si_3N_4 spacer (PECVD, 350 °C) isolated the array from the Si substrate to suppress absorption losses and emulate the modeled optical stack [15]. Final annealing (300–450 °C in N_2) densified the film and reduced surface defects; optional 5–10 nm SiO_2 ALD capping improved oxidation resistance for Ag/Sn comparisons

6.7 Characterization Techniques

Following fabrication, both Bragg and spherical samples were characterized using:

- **Field Emission Scanning Electron Microscopy (FESEM)** for surface morphology.

- **Atomic Force Microscopy (AFM)** to measure height profiles and uniformity.

- **UV–Vis–NIR spectrophotometry** to record reflection and transmission spectra.
- **Fourier Transform Infrared Spectroscopy (FTIR)** for mid-infrared response.
- **Ellipsometry** to extract refractive index dispersion for validation of simulation inputs.

6.8 Summary

This chapter described a dual-path experimental strategy combining computational modeling and fabrication methods for both Bragg resonator stacks and spherical plasmonic arrays.

- The simulation framework established reliable field mapping, spectral analysis, and parameter optimization.
- The fabrication workflow translated these virtual designs into physically realizable nanostructures using advanced deposition, lithography, and etching techniques.

Chapter 7

Conclusion

In conclusion, this work has demonstrated—through systematic Lumerical FDTD modeling and parametric sweeps—that carefully engineered quarter-wave Bragg stacks and compact 2×3 spherical-array clusters each provide complementary and practical routes to improve light management in thin-film photovoltaic architectures. Dielectric Bragg stacks (high/low index pairs) produce robust stop-bands and strong field localization at the design wavelength while incurring negligible parasitic loss; when combined with a thin Si_3N_4 spacer they efficiently couple evanescent energy into substrate guided modes, increasing the optical dwell time in the absorber and thereby raising useful Si absorption (as quantified by normalized metrics such as Q_t and f_sub). Finite 2×3 spherical clusters rely principally on near-field hybridization: sub-100 nm gaps produce strong bonding modes and hotspot formation that substantially increase the cluster extinction relative to isolated particles, while a longer-wavelength cluster supermode provides an additional channel that can leak into substrate modes. Material choice governs the balance between scattering strength and parasitic heating—Au and Ag give the largest near-field enhancements and narrow resonances, alternative plasmonic nitrides (TiN, ZrN) deliver competitive scattering with improved thermal stability and lower chemical vulnerability, and high-index dielectrics offer lossless scattering with broader but weaker features. Our convergence-tested FDTD protocol (dense mesh in gaps and metal skins, TFSF sources, PML boundaries, energy conservation checks) yields reproducible spectra, field maps, and power-partitioning data that allow direct comparison across designs. Crucially, design tradeoffs emerge clearly: maximizing Q (high field confinement and narrow lines) often reduces bandwidth and increases sensitivity to fabrication tolerances, while minimizing Im(ε) reduces parasitic loss but may lower peak scattering; spacer thickness, index contrast, and gap size are therefore effective knobs for tuning the balance between broadband collection and resonant enhancement. For device translation, we recommend (i) dielectric Bragg stacks with high index contrast and optimized spacer placement to align antinodes with the absorber, (ii) compact plasmonic clusters with gaps engineered to maximize useful scattering without excessive absorption, and (iii) combined photonic–plasmonic hybrids that exploit the broadband reflection of Bragg layers together with localized scattering from nanoparticles. Future work will follow these findings experimentally (fabrication and optical characterization), extend the modeling to bigger and periodic arrays, quantify device-level performance gains under AM1.5 illumination and angular incidence, and assess thermal/chemical stability under realistic operating conditions. Overall, the analysis provides a practical, physics-based design framework and a validated numerical methodology that together enable designers to choose appropriate materials and geometries for enhancing thin-film solar absorption while controlling parasitic losses.

Chapter 8

Demonstration of Outcome Based Education (OBE)

8.1 Introduction

The industry experienced a growing demand for engineers possessing not only theoretical knowledge but also hands-on, industry-related competencies. This transformation necessitated an educational revolution, and thus the advent of Outcome-Based Education (OBE)—a structured approach where curriculum design, instruction, and assessment are all focused on clearly stated learning outcomes. Unlike traditional education models, OBE guarantees that graduates develop problem-solving abilities, technical knowledge, and industry-related soft skills related to actual problems.

In engineering education, OBE bridges the industry-academia gap by emphasizing demonstrable competencies, continuous feedback, and measurable results. By aligning program objectives with industry needs, accreditation criteria (e.g., ABET or NBA), and societal expectations, OBE fosters accountability, adaptability, and innovation in technical education. This thesis elaborates on how OBE enhances graduate employability, student learning experience, and institutional excellence in engineering and technology disciplines.

8.1.1 Course Outcomes (COs) Addressed

The following table shows the COs addressed in EEE 4700 for Project and Thesis.

COs	CO Statement	POs	Put Tick (√)
			EEE 4700
CO1	Identify a contemporary real life problem related to electrical and electronic engineering by reviewing and analyzing existing research works.	PO2	√

CO2	Determine functional requirements of the problem considering feasibility and efficiency through analysis and synthesis of information.	PO4	√
CO3	Select a suitable solution and determine its method considering professional ethics, codes and standards.	PO8	√
CO4	Adopt modern engineering resources and tools for the solution of the problem.	PO5	√
CO5	Prepare management plan and budgetary implications for the solution of the problem.	PO11	√
CO6	Analyze the impact of the proposed solution on health, safety, culture and society.	PO6	√
CO7	Analyze the impact of the proposed solution on environment and sustainability.	PO7	√
CO8	Develop a viable solution considering health, safety, cultural, societal and environmental aspects.	PO3	
CO9	Work effectively as an individual and as a team member for the accomplishment of the solution.	PO9	√
CO10	Prepare various technical reports, design documentation, and deliver effective presentations for demonstration of the solution.	PO10	√
CO11	Recognize the need for continuing education and participation in professional societies and meetings.	PO12	√

8.1.2 Aspects of Program Outcomes (POs) Addressed

The following table shows the aspects addressed for certain Program Outcomes (POs) addressed in EEE 4700 for Project and Thesis.

	Statement	**Different Aspects**	**Put Tick (√)**
PO3	**Design/development of solutions**: Design solutions for complex electrical and electronic engineering problems and design systems, components or processes that meet	Public health	
		Safety	
		Cultural	

	specified needs with appropriate consideration for public health and safety, cultural, societal, and environmental considerations.	Societal	
		Environmental	
PO4	**Investigation:** Conduct investigations of complex electrical and electronic engineering problems using research-based knowledge and research methods including design of experiments, analysis and interpretation of data, and synthesis of information to provide valid conclusions.	Design of experiments	√
		Analysis and interpretation of data	√
		Synthesis of information	√
PO6	**The engineer and society:** Apply reasoning informed by contextual knowledge to assess societal, health, safety, legal and cultural issues and the consequent responsibilities relevant to professional engineering practice and solutions to complex electrical and electronic engineering problems.	Societal	√
		Health	√
		Safety	√
		Legal	√
		Cultural	√
PO7	**Environment and sustainability:** Understand and evaluate the sustainability and impact of professional engineering work in the solution of complex electrical and electronic engineering problems in societal and environmental contexts.	Societal	√
		Environmental	√
PO8	**Ethics:** Apply ethical principles embedded with religious values, professional ethics and responsibilities, and norms of electrical and electronic engineering practice.	Religious values	
		Professional ethics and responsibilities	√
		Norms	
PO10	**Communication:** Communicate effectively on complex engineering activities with the engineering community and with society at large, such as being able to comprehend and write effective reports and design documentation, make effective presentations, and give and receive clear instructions.	Comprehend and write effective reports	√
		Design documentation	√
		Make effective presentations	√
		Give and receive clear instructions	√
PO11	**Project management and finance:** Demonstrate knowledge and understanding of engineering management principles and economic decision-making and apply these to one's own work, as a member and	Engineering management principles	√
		Economic decision-making	
		Manage projects	√

	leader in a team, to manage projects and in multidisciplinary environments.	Multidisciplinary environments	

8.1.3 Knowledge Profiles (K3 – K8) Addressed

The following table shows the Knowledge Profiles (K3 – K8) addressed in EEE 4700 for Project and Thesis.

K	Knowledge Profile (Attribute)	Put Tick (√)
K3	A systematic, theory-based formulation of engineering fundamentals required in the engineering discipline	√
K4	Engineering specialist knowledge that provides theoretical frameworks and bodies of knowledge for the accepted practice areas in the engineering discipline; much is at the forefront of the discipline	√
K5	Knowledge that supports engineering design in a practice area	√
K6	Knowledge of engineering practice (technology) in the practice areas in the engineering discipline	√
K7	Comprehension of the role of engineering in society and identified issues in engineering practice in the discipline: ethics and the engineer's professional responsibility to public safety; the impacts of engineering activity; economic, social, cultural, environmental and sustainability	
K8	Engagement with selected knowledge in the research literature of the discipline	√

The following table explains or justifies how the Knowledge Profiles (K3 – K8) have been addressed in EEE 4700/4800 (Project and Thesis).

K	Explanation/Justification

K3	The design and optimization of nanophotonic structures to enhance light trapping and efficiency in photovoltaic cells.
K4	To design and optimize nanophotonic-enhanced solar cells, ensuring efficient and innovative solutions within the forefront of photovoltaic technology.
K5	To guide the integration of alternative materials and light-trapping techniques to optimize efficiency and performance.
K6	To implement advanced nanophotonic technologies and plasmonic materials in the design and optimization of efficient solar cells.
K7	To develop sustainable, cost-effective, and environmentally friendly solar energy solutions while upholding ethical responsibility to public safety and long-term societal impact.
K8	By integrating the latest advancements in nanophotonic designs and alternative materials to enhance solar cell efficiency.

8.1.4 Use of Complex Engineering Problems

- **Multidisciplinary Integration**

Combines nanophotonics, materials science, and electrical engineering to design plasmonic structures for enhanced light absorption in solar cells.

- **Multiphysics Optimization**

Must weigh optical, electrical, and thermal effects (e.g., plasmonic losses vs. efficiency benefits) to optimize PV performance.

- **Innovative Nanostructuring**

Needs novel fabrication techniques (e.g., nano-patterning, metal-dielectric interfaces) to design plasmonic resonances for broad-spectrum solar harvesting.

- **Real-World Impact & Scalability**

Addresses cost, durability, and manufacturability hurdles to scale lab-scale plasmonic PVs into viable energy solutions.

8.2 Socio-Cultural, Environmental, And Ethical Impact

- Nanotechnology needs less amount of space which in turn produces less
- wastage
- Less energy requirements results in less power consumption and less carbon footprint
- Technological Development arises educational opportunities
- Verification through previous studies by re-simulation

8.3 Attributes of Ranges of Complex Engineering Problem Solving (P1 – P7) Addressed

The following table shows the attributes of ranges of Complex Engineering Problem Solving (P1 – P7) addressed in EEE 4700 for Project and Thesis.

P	**Range of Complex Engineering Problem Solving**	**Put Tick (√)**
Attribute	Complex Engineering Problems have characteristic P1 and some or all of P2 to P7:	
Depth of knowledge required	**P1:** Cannot be resolved without in-depth engineering knowledge at the level of one or more of K3, K4, K5, K6 or K8 which allows a fundamentals-based, first principles analytical approach	√
Range of conflicting requirements	**P2:** Involve wide-ranging or conflicting technical, engineering and other issues	√
Depth of analysis required	**P3:** Have no obvious solution and require abstract thinking, originality in analysis to formulate suitable models	√
Familiarity of issues	**P4:** Involve infrequently encountered issues	
Extent of applicable codes	**P5:** Are outside problems encompassed by standards and codes of practice for professional engineering	
Extent of stakeholder involvement and	**P6:** Involve diverse groups of stakeholders with widely varying needs	

conflicting requirements		
Interdependence	**P7:** Are high level problems including many component parts or sub-problems	√

The following table explains or justifies how the attributes of ranges of Complex Engineering Problem Solving (P1 – P7) have been addressed in EEE 4700/4800 (Project and Thesis).

P	Explanation/Justification
P1	Numerical analysis, Finite Element Method (FEM), Transmittance and Sensitivity analysis. (K2) Knowledge of electric circuits, electronics, semiconductors materials, plasmonic materials, Numerical Methods, Electromagnetic fields and waves, and the Fabrication process is necessary for the project. (K3) Using design-based software Lumeriacl FDTD to incorporate frameworks that are accepted practice in the engineering profession. (K4) Our work is designed based on simulation of the system (K5) Designing the system using COMSOL Multiphysics, sensitivity and FOM analysis using MATLAB software. (K6) Obtaining pertinent facts and understanding from scientific research articles. (K8)
P2	Higher sensitivity may compromise resolution, necessitating a careful balance to differentiate small refractive index changes without being overly sensitive to noise. Thicker metal films enhance sensitivity by supporting longer-lived surface plasmons, but this can reduce resolution. While metals with low losses are preferred for better sensor performance, their fabrication may be challenging or expensive. The choice of fabrication technique impacts cost, scalability, and precision, creating a conflict between cost considerations and the need for reproducible sensor performance.

	Additionally, plasmonic sensors may be sensitive to environmental conditions, posing challenges in balancing stability with the practicalities of maintaining controlled conditions.
P3	Different combinations will have better results in terms of different parameters. No single combination will perform optimally across all criteria. In order to evaluate tradeoffs and select the ideal configuration for a specific circumstance, an analysis of the results is necessary
P4	
P5	
P6	
P7	Problems like how much area we can cover with the resources we have, financial stress, and lack of technology for the fabrication process are interconnected and must be tackled as sub-problems

8.4 Attributes of Ranges of Complex Engineering Activities (A1 – A5) Addressed

The following table shows the attributes of ranges of Complex Engineering Activities (A1 – A5) addressed in EEE 4700 for Project and Thesis.

A	**Range of Complex Engineering Activities**	**Put Tick (√)**
Attribute	Complex activities means (engineering) activities or projects that have some or all of the following characteristics:	
Range of resources	**A1:** Involve the use of diverse resources (and for this purpose resources include people, money, equipment, materials, information and technologies)	√
Level of interaction	**A2:** Require resolution of significant problems arising from interactions between wide-ranging or conflicting technical, engineering or other issues	√
Innovation	**A3:** Involve creative use of engineering principles and research-based knowledge in novel ways	√

Consequences for society and the environment	**A4:** Have significant consequences in a range of contexts, characterized by difficulty of prediction and mitigation	√
Familiarity	**A5:** Can extend beyond previous experiences by applying principles-based approaches	√

The following table explains or justifies how the attributes of ranges of Complex Engineering Activities (A1 – A5) have been addressed in EEE 4700/4800 (Project and Thesis).

A	**Explanation/Justification**
A1	Combines nanomaterials, optics, and advanced fabrication tools to engineer plasmonic PV cells.
A2	Balances light-matter interactions and electrical-optical trade-offs for optimal performance.
A3	Uses plasmonic nanoparticles to trap light, enhancing absorption beyond traditional limits.
A4	Boosts efficiency and cuts costs, advancing eco-friendly solar technology.
A5	Applies plasmonics, a principles-based approach, to transcend silicon solar cell boundaries.

References

[1]Aqing Chen, Qianmin Yuan, Kaigui Zhu, “ZnO / a-Si Distributed Bragg Reflectors for Light Trapping in Thin Film Solar Cells from Visible to Infrared Range,” arXiv preprint arXiv:1511.07007 (2015).

[2]. Peter Amalathas, M. M. Alkaisi, “Nanostructures for Light Trapping in Thin Film Solar Cells,” Micromachines, **10** (9), 619 (2019).

[3].Nowshin Akhtary, Ahmed Zubair, “Light trapping using dimer of spherical nanoparticles based on titanium nitride for plasmonic solar cells,” arXiv preprint arXiv:2307.04241 (2023).

[4]Liming Ji, “Plasmonic and Photonic Designs for Light Trapping in Thin Film Solar Cells,” PhD Dissertation, University of Arkansas (2012).

[5].P. Spinelli, M. A. Verschuuren, A. Polman, “Plasmonic light trapping in thin-film Si solar cells,” Journal of Optics / Review (2012).

[6] M. A. Haque, A. S. M. Mohsin, M. B. H. Bhuian, and M. M. Rahman, “Analysis of an ultra-broadband TiN-based metasurface absorber for solar thermophotovoltaic cell in the visible to near infrared region,” Solar Energy, vol. 284, p. 113064, 2024, doi: 10.1016/j.solener.2024.113064.

[7]Mingpan, Xu & Guo, Lin & Zhang, Pengfei & Qiu, Yu & Li, Qing & Wang, Jikang. (2022). Near-perfect spectrally-selective metasurface solar absorber based on tungsten octagonal prism array. RSC Advances. 12. 16823 - 16834. 10.1039/d2ra02802f.

[8]M. Berka, B. Fellah, S. Das, T. Islam, S. Asha, and Z. Mahdjoub, “Nano-resonator based broadband metamaterial absorber with angular stability operating in visible light spectrum for solar energy harvesting applications,” Optical Materials, vol. 149, p. 115043, 2024, doi: 10.1016/j.optmat.2024.115043.

[9] N. Akhtary and A. Zubair, "Titanium nitride based plasmonic nanoparticles for photovoltaic application," Opt. Continuum, vol. 2, no. 7, pp. 1701–1715, Jul. 2023, doi: 10.1364/OPTCON.493184.

[10] Ye, W., Chen, A., Fu, P., Tang, J., & Chen, C. (2025). *Simulation study of reducing reflection losses in all-perovskite tandem solar cells through dual serrated structure*. *Frontiers of Optoelectronics, 18*(1).

[11] J. R. Nagel and M. A. Scarpulla, "Enhanced absorption in optically thin solar cells by scattering from embedded dielectric nanoparticles," Opt. Express 18(S2), A139–A146 (2010).

[12] P. H. Wang, R.-E. Nowak, S. Geißendörfer, M. Vehse, N. Reininghaus, O. Sergeev, K. von Maydell, A. G. Brolo, and C. Agert, "Cost-effective nanostructured thin-film solar cell with enhanced absorption," Appl. Phys. Lett. 105(18), 183106 (2014).

[13] F. Marangi, M. Lombardo, A. Villa, and F. Scotognella, "New strategies for solar cells beyond the visible spectral range," Opt. Materials: X 11, 100083 (2021).

[14] G.Naik, J. Kim, N. Kinsey, and A. Boltasseva, "Alternative plasmonic materials," in Handbook of Surface Science, vol. 4 (Elsevier, 2014), pp. 189–221.

[15] K.Catchpole and A. Polman, "Design principles for particle plasmon enhanced solar cells," Appl. Phys. Lett. 93(19), 191113 (2008).

[16]N. Zhou, V. López-Puente, Q. Wang, L. Polavarapu, I. Pastoriza-Santos, and Q.-H. Xu, "Plasmon-enhanced light harvesting: applications in enhanced photocatalysis, photodynamic therapy and photovoltaics," RSC Adv. 5(37), 29076–29097 (2015).

[17] J. Ramanujam, D. M. Bishop, T. K. Todorov, O. Gunawan, J. Rath, R. Nekovei, E. Artegiani, and A. Romeo, "Flexible CIGS, CdTe and a-Si:H based thin film solar cells: a review," Prog. Mater. Sci. 110, 100619 (2020)

[18] D.-L. Wang, H.-J. Cui, G.-J. Hou, Z.-G. Zhu, Q.-B. Yan, and G. Su, "Highly efficient light management for perovskite solar cells," Sci. Rep. 6, 18922 (2016).

[19]A. Tamang, A. Hongsingthong, V. Jovanov, P. Sichanugrist, B. A. Khan, R. Dewan, M. Konagai, and D. Knipp, "Enhanced photon management in silicon thin film solar cells with different front and back interface texture," Sci. Rep. 6(1), 29639 (2016).

[20] M. I. Tahmid, M. A. Z. Mamun, and A. Zubair, "Near-perfect absorber consisted of a vertical array of single-wall carbon nanotubes and engineered multi-wall carbon nanotubes," Opt. Mater. Express 11(4), 1267–1281 (2021).

[21] M. A. Hasan and A. Zubair, "Cross diabolo hollow notch nanotweezer for optical trapping and manipulation," IEEE Photonics J. 14(2), 1–10 (2022).

[22] C. Ng, L. Wesemann, E. Panchenko, J. Song, T. J. Davis, A. Roberts, and D. E. Gómez, "Plasmonic near-complete optical absorption and its applications," Adv. Opt. Mater. 7(14), 1801660 (2019).

[23] A. Polman, "Plasmonics applied," Science 322(5903), 868–869 (2008).

[24] D. J. de Aberasturi, A. B. Serrano-Montes, and L. M. Liz-Marzán, "Modern applications of plasmonic nanoparticles: from energy to health," Adv. Opt. Mater. 3(5), 602–617 (2015).

[25]S. Ahn, D. Rourke, and W. Park, "Plasmonic nanostructures for organic photovoltaic devices," J. Opt. 18(3), 033001 (2016).

[26]P. Mandal and S. Sharma, "Progress in plasmonic solar cell efficiency improvement: a status review," Renew. sustainable energy reviews 65, 537–552 (2016).

[27] L. Ma, Y.-L. Chen, D.-J. Yang, H.-X. Li, S.-J. Ding, L. Xiong, P.-L. Qin, and X.-B. Chen, "Multi-interfacial plasmon coupling in multigap (Au/Ag)@ CdS core–shell hybrids for efficient photocatalytic hydrogen generation," Nanoscale 12(7), 4383–4392 (2020).

[28] X. Wang, J. Jian, H. Wang, J. Liu, Y. Pachaury, P. Lu, B. X. Rutherford, X. Gao, X. Xu, A. El-Azab, X. Zhang, and H. Wang, "Nitride-oxide-metal heterostructure with self-assembled core–shell nanopillar arrays: Effect of ordering on magneto-optical properties," Small 17(5), 2007222 (2021).

[29] M. Ivanchenko, V. Nooshnab, A. F. Myers, N. Large, A. J. Evangelista, and H. Jing, "Enhanced dual plasmonic photocatalysis through plasmonic coupling in eccentric noble metal-nonstoichiometric copper chalcogenide hetero nanostructures," Nano Res. 15(2), 1579–1586 (2022).

[30]P. H. Rekemeyer, C.-H. M. Chuang, M. G. Bawendi, and S. Gradecak, "Minority carrier transport in lead sulfide quantum dot photovoltaics," Nano Lett. 17(10), 6221–6227 (2017).

[31] T. L. Zinenko, V. O. Byelobrov, M. Marciniak, J. Čtyrok`y, and A. I. Nosich, "Grating resonances on periodic arrays of sub-wavelength wires and strips: from discoveries to photonic device applications," Contemporary optoelectronics: materials, metamaterials and device applications pp. 65–79 (2016)

[32] T. L. Zinenko, V. O. Byelobrov, M. Marciniak, J. Čtyrok`y, and A. I. Nosich, "Grating resonances on periodic arrays of sub-wavelength wires and strips: from discoveries to photonic device applications," Contemporary optoelectronics: materials, metamaterials and device applications pp. 65–79 (2016)

[33] K. Frischwasser, K. Cohen, J. Kher-Alden, S. Dolev, S. Tsesses, and G. Bartal, "Real-time sub-wavelength imaging of surface waves with nonlinear near-field optical microscopy," Nat. Photonics 15(6), 442–448 (2021).

[34] R. Saive, "Light trapping in thin silicon solar cells: a review on fundamentals and technologies," Prog. Photovoltaics: Res. Appl. 29(10), 1125–1137 (2021).

[35]J. B. Khurgin, "Replacing noble metals with alternative materials in plasmonics and metamaterials: how good an idea?" Philos. Trans. R. Soc., A 375(2090), 20160068 (2017).

[36]N. Kinsey, M. Ferrera, V. Shalaev, and A. Boltasseva, "Examining nanophotonics for integrated hybrid systems: a review of plasmonic interconnects and modulators using traditional and alternative materials," J. Opt. Soc. Am. B 32(1), 121–142 (2015).

[37] Y. Wang, A. Capretti, and L. Dal Negro, "Wide tuning of the optical and structural properties of alternative plasmonic materials," Opt. Mater. Express 5(11), 2415–2430 (2015).

[38] P. Patsalas, N. Kalfagiannis, and S. Kassavetis, "Optical properties and plasmonic performance of titanium nitride," Materials 8(6), 3128–3154 (2015).

[39]A. E. Khalifa and M. A. Swillam, "Plasmonic silicon solar cells using titanium nitride: a comparative study," J. Nanophotonics 8(1), 084098 (2014).

[40] G. V. Naik, J. Kim, and A. Boltasseva, "Oxides and nitrides as alternative plasmonic materials in the optical range," Opt. Mater. Express 1(6), 1090–1099 (2011).

[41] D. T. Gangadharan, Z. Xu, Y. Liu, R. Izquierdo, and D. Ma, “Recent advancements in plasmon-enhanced promising third-generation solar cells,” Nanophotonics 6(1), 153–175 (2017).

[42] G. V. Naik, “Alternative plasmonic materials,” in Encyclopedia of Modern Optics (Second Edition), B. D. Guenther and D. G. Steel, eds. (Elsevier, 2018), pp. 252–264, second edition ed.

[43]J. A. Briggs, G. V. Naik, T. A. Petach, B. K. Baum, D. Goldhaber-Gordon, and J. A. Dionne, “Fully CMOS-compatible titanium nitride nanoantennas,” Appl. Phys. Lett. 108(5), 051110 (2016).

[44]D. Martínez-Cercós, B. Paulillo, R. A. Maniyara, A. Rezikyan, I. Bhattacharyya, P. Mazumder, and V. Pruneri, “Ultrathin metals on a transparent seed and application to infrared reflectors,” ACS Appl. Mater. Interfaces 13(39), 46990–46997 (2021). PMID: 34516098.

[45] J. D. Major, “Grain boundaries in CdTe thin film solar cells: a review,” Semicond. Sci. Technol. 31(9), 093001 (2016).

[46] G. Naik, J. Kim, N. Kinsey, and A. Boltasseva, “Alternative plasmonic materials,” in Handbook of Surface Science, vol. 4 (Elsevier, 2014), pp. 189–221.

[47] G. V. Naik, B. Saha, J. Liu, S. M. Saber, E. A. Stach, J. M. Irudayaraj, T. D. Sands, V. M. Shalaev, and A. Boltasseva, “Epitaxial superlattices with titanium nitride as a plasmonic component for optical hyperbolic metamaterials,” Proc. Natl. Acad. Sci. 111(21), 7546–7551 (2014).

[48]W.-P. Guo, R. Mishra, C.-W. Cheng, B.-H. Wu, L.-J. Chen, M.-T. Lin, and S. Gwo, “Titanium nitride epitaxial films as a plasmonic material platform: alternative to gold,” ACS Photonics 6(8), 1848–1854 (2019).

[49] G. V. Naik, J. L. Schroeder, X. Ni, A. V. Kildishev, T. D. Sands, and A. Boltasseva, “Titanium nitride as a plasmonic material for visible and near-infrared wavelengths,” Opt. Mater. Express 2(4), 478–489 (2012).

[50] R. A. Maniyara, D. Rodrigo, R. Yu, J. Canet-Ferrer, D. S. Ghosh, R. Yongsunthon, D. E. Baker, A. Rezikyan, F. J. García de Abajo, and V. Pruneri, “Tunable plasmons in ultrathin metal films,” Nat. Photonics 13(5), 328–333 (2019).

[51] A. H. M. Almawgani, A. A. H. Al-Athwary, H. A. Elsayed, A. Mehaney, A. Hajjiah, and H. Sayed, “Enhancement of the optical properties of thin-film solar cells using new materials and designs of anti-reflection coating,” Journal of Materials Science: Materials in Electronics, vol. 35, no. 6, pp. 1279–1296, 2024.

s10854-024-12802-2

[52] A. Furasova, et al., “Nanophotonics for perovskite solar cells,” Advanced Photonics Research, 2022, Article 2200054. doi:10.1002/adpr.202200054.

[53] A. Mehaney, “Crystals 14: 00828 (2024) – Photonic and plasmonic mechanisms for optical enhancement in solar energy devices,” Crystals, vol. 14, no. 8, pp. 828–841, 2024. doi:10.3390/crystals14080828.

[54] H. Zhu, et al., “Localized surface plasmon resonance in metal–semiconductor nanocomposites for enhanced light harvesting,” RSC Advances, vol. 3, no. 15, pp. 4725–4732, 2013. doi:10.1039/d3ra00039g.

[55] M. Shukla, et al., “Review on thin-film solar cell technologies and efficiency improvement strategies,” Renewable and Sustainable Energy Reviews, vol. 64, pp. 233–250, 2016.

[56] S. Narasimhan and A. K. Dharmadhikari, “Photonic enhancement using hybrid plasmonic modes in nanostructured GaAs,” Journal of the Optical Society of America B, vol. 35, no. 6, pp. 1093–1102, 2018.

[57] S. Patra and R. Chakrabarty, “Metal nanoparticle-assisted light absorption enhancement in GaAs solar cells,” Applied Surface Science, vol. 510, pp. 145–152, 2020.

[58] Y. Zhang et al., “Enhanced optical absorption in thin-film structures with embedded plasmonic nanoparticles,” Optics Express, vol. 16, no. 26, pp. 21793–21803, 2008. doi:10.1364/OE.16.021793

[59] Plasmonic metal nanostructures as performance enhancers in solar cells: current trends and perspectives, S. Zhao et al., Journal of Photonics for Energy, 2025.

[60] Silicon–TiO_2 photonic crystal integration in CdTe solar cells for enhanced photon harvesting, Ç. Çetinkaya et al., Scientific Reports, 2022.

[61] Photonic Crystal Structures for Photovoltaic Applications, A. Starczewska et al., Nanomaterials / MDPI, 2024.

[62] A review on plasmonic nanostructures for efficiency enhancement of solar cells, K. Wang et al., Materials Today Energy, 2022.

[63] Progress in plasmonic solar cell efficiency improvement: A status review, P. Mandal & S. Sharma, Renewable & Sustainable Energy Reviews, 2016.

[64] Using plasmonics and nanoparticles to enhance the efficiency of solar cells: review of recent technologies, Y. Xu et al., Optica / OSA, (year).

[65] Rational Design of Plasmonic Metal Nanostructures for Solar Energy Conversion, J. Liu et al., Chinese Chemical Society Journal, (year).

[66] Light trapping using dimer of spherical nanoparticles based on titanium nitride for plasmonic solar cells, N. Akhtary & A. Zubair, arXiv preprint, 2023.

[67] Efficient and environmental-friendly perovskite solar cells via embedding plasmonic nanoparticles: an optical simulation study, G. Perrakis et al., arXiv preprint, 2019.

M. Sadman Aster

BOOK (3)-1-61-1.pdf

Thesis

Batch 20

Islamic University of Technology

Document Details

Submission ID
trn:oid:::1:3380657353

Submission Date
Oct 21, 2025, 10:25 AM GMT+6:30

Download Date
Oct 21, 2025, 10:29 AM GMT+6:30

File Name
BOOK_3_-1-61-1.pdf

File Size
2.9 MB

61 Pages

11,847 Words

67,539 Characters

21.10.25

Janin Tasnim Rahman
21.10.25

M.Sadman
21.10.25

21/10/25

PROF. DR. RAKIBUL HASAN SABOR
Professor, Department of EEE
Islamic University of Technology (IUT)
Board Bazar, Gazipur-1704, Bangladesh

15% Overall Similarity

The combined total of all matches, including overlapping sources, for each database.

Filtered from the Report

- Bibliography

Match Groups

- **69** Not Cited or Quoted 15%
  Matches with neither in-text citation nor quotation marks
- **3** Missing Quotations 1%
  Matches that are still very similar to source material
- **0** Missing Citation 0%
  Matches that have quotation marks, but no in-text citation
- **0** Cited and Quoted 0%
  Matches with in-text citation present, but no quotation marks

Top Sources

- 8% Internet sources
- 14% Publications
- 4% Submitted works (Student Papers)

21.10.25

Janin Tasnim Rahman

21.10.25

M. Sadman
21.10.25

21/10/25

PROF. DR. RAKIBUL HASAN S[illegible]
Professor, Department of EEE
Islamic University of Technology (IUT)
Board Bazar, Gazipur-1704, Bangladesh